J. Fluid Mech. (1997), *vol.* 335, *pp.* 323–359

Three-dimensional ribbing instability in symmetric forward-roll film-coating processes

By MARIANO E. GURFINKEL CASTILLO† AND ANTHONY T. PATERA‡

Department of Mechanical Engineering, Room 3-266, Massachusetts Institute of Technology, Cambridge, MA 02139, USA

(Received 5 September 1994 and in revised form 18 September 1996)

We propose a framework for interpreting the formation, evolution, and spatial persistence of ribbing in coating processes, and present companion 'quantifying' parallel spectral element simulations of fully nonlinear unsteady three-dimensional free-surface symmetric forward-roll film-coating fluid flows. The framework couples, by means of a transition region, two well-understood phenomena: the 'viscous fingering' instability of a splitting meniscus; and the levelling of viscous films under the effect of surface tension. The transition-region length, L_t, is on the order of the coating film thickness, while the downstream extent of the levelling region – the distance over which ribs persist – L_ℓ, depends on the fluid properties, the flow conditions, and the wavenumber content of the nonlinear meniscus rib profile. Numerical results are presented for the evolution of the coating flow from perturbed unstable two-dimensional steady states to three-dimensional saturated ribbed states for several representative supercritical capillary numbers, Ca, and spanwise periodicity lengths, b. Nonlinear state selection is briefly discussed.

1. Introduction

The coating of continuous webs is an important manufacturing process which finds wide application in the photographic and publishing industries. Although much effort has been devoted to developing and studying processes for the production of uniform films, a major cause of defects – the three-dimensional hydrodynamic phenomenon known as 'ribbing' or 'ribbing-line instability' – is not yet completely understood. Ribbing is characterized by a spanwise waviness of the film free surface (Pitts & Greiller 1961; Ruschak 1985; Coyle, Macosko & Scriven 1990*b*) that extends downstream with the web, and that, in most applications, renders the finished product useless.

1.1. *Brief summary of previous work*

In this paper we study ribbing in the symmetric forward-roll coating device depicted in figure 1. In the forward-roll coating process, two counter-rotating rollers entrain and meter fluid onto a web. During normal operation, a continuous uniform film is produced; however, if the speed of rotation of the rollers or the viscosity of the fluid is increased, or if the surface tension of the fluid–gas interface is decreased,

† Present address: Intevep S.A., POBOX 76343, Caracas Venezuela 1070A.
‡ Author to whom correspondence should be addressed.

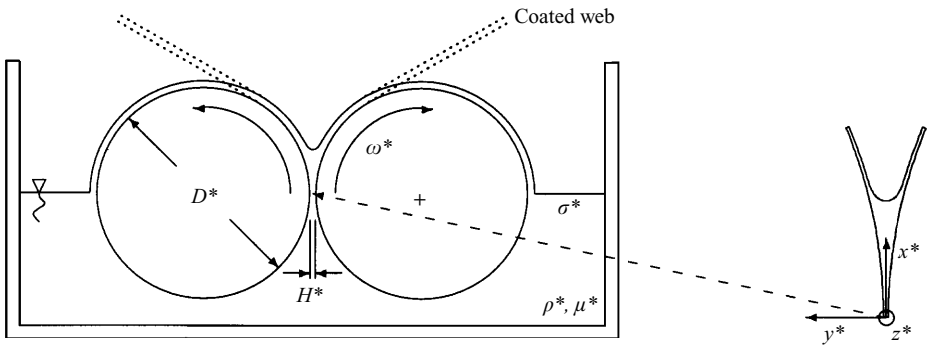

FIGURE 1. Schematic of a symmetric forward-roll film-coating device: two rollers of diameter D^*, counter-rotating at angular speed ω^*, entrain fluid of viscosity μ^*, density ρ^*, and surface tension σ^*, through a metering gap of width H^*.

ribs appear and persist downstream on the film (Pitts & Greiller 1961; Dowson & Taylor 1979; Ruschak 1985; Coyle *et al.* 1990*b*). The rotating speeds for which ribbing is encountered in symmetric forward-roll coating are uneconomically slow, and thus other industrial coating processes have been developed and studied. These other processes (Kistler & Scriven 1983; Ruschak 1985; Christodolou & Scriven 1989; Coyle, Macosko & Scriven 1990*a*; Cohen & Gutoff 1992; Coyle 1992; Lee, Liu & Liu 1992; Gutoff 1993) may also exhibit ribbing, but typically at higher coating speeds. We choose to study ribs in forward-roll coating because, first, we avoid the complication of static or dynamic contact lines (Dussan V. & Davis 1986; Saffman 1986; Kistler & Scriven 1994), and second, ribs are readily obtained and constitute the principal defect.

Linear stability theory accurately identifies the onset of ribbing as the growth of infinitesimal three-dimensional disturbances to two-dimensional steady but unstable base states (Pearson 1960; Pitts & Greiller 1961; Mill & South 1967; Ruschak 1983; Coyle *et al.* 1990*b*; Rabaud, Couder & Michalland 1991). Lubrication theory and matched asymptotic expansions predict the two-dimensional base states in the limit of vanishing gap to roll diameter ratio, $H^*/D^* \to 0$, in which the inner problem reduces to the splitting flow between two parallel plates (Ruschak 1983; Coyle, Macosko & Scriven 1986). (Here, and in what follows, superscript * indicates a dimensional quantity.) For arbitrary H^*/D^*, numerical approaches must be considered owing to the two-dimensionality of the flow field and the free-surface-induced nonlinearity. Coyle *et al.* (1986) combine the finite-element method and Newton-iteration solution procedure to compute two-dimensional flow geometries and flow fields for forward-roll coating for a wide range of H^*/D^*; their reported results are in very good agreement with experiment (Decré, Gailly & Buchlin 1995).

On the basis of these two-dimensional states, Ruschak (1983), for small H^*/D^*, and Coyle *et al.* (1990*b*), for general H^*/D^*, present numerical solutions to the eigenvalue problem for the growth rate of infinitesimal three-dimensional disturbances. For a fixed D^*/H^*, the stability of the two-dimensional base states with respect to three-dimensional disturbances of given spanwise wavelength, λ^*, is determined by the capillary number $Ca = \mu^* V^*/\sigma^*$, where μ^*, σ^*, and $V^* = \omega^* D^*/2$ are the viscosity and surface tension of the fluid, and the tangential velocity of the rollers, respectively. The critical capillary number, Ca_c, for a given geometry, D^*/H^*, is defined as the minimum capillary number, Ca, for which the greatest growth rate over all disturbance

wavelengths, λ^*, vanishes. The associated critical eigenfunction has a wavelength, λ_c^*, and a wavenumber, β_c, related by $\beta_c \equiv \pi H^*/\lambda_c^*$ (note we non-dimensionalize the wavenumber with respect to the half-gap, $H^*/2$). The linear stability results presented by Coyle *et al.* (1990*b*) are in very good agreement with experimental observations for the onset of ribbing (Pitts & Greiller 1961; Mill & South 1967; Benkreira, Edwards & Wilkinson 1982; Coyle *et al.* 1990*b*), confirming that the instability – disregarding imperfections such as end effects – is a supercritical bifurcation. Linear stability theory indicates that, for supercritical capillary numbers, $Ca > Ca_c$, a continuous range of wavenumbers $[\beta_L(Ca), \beta_H(Ca)]$ is unstable, where $\beta_L(Ca)$ and $\beta_H(Ca)$ are the low- and high-wavenumber cutoffs, respectively (Coyle *et al.* 1990*b*).

The description of the mechanism for ribbing dates back to the work of Pearson (1960) and Pitts & Greiller (1961); other descriptions are given by Savage (1977), Ruschak (1985), Hakim *et al.* (1990), Rabaud *et al.* (1991), and Coyle (1992). Briefly stated, the splitting meniscus and roller curvature cause a non-negative pressure gradient normal to the meniscus free surface; from arguments forwarded by Saffman & Taylor (1958) to explain viscous fingering, it can then be shown that, in the presence of this positive pressure gradient normal to the free surface, and in the absence of surface tension, disturbances to the free surface tend to grow (Pearson 1960; Pitts & Greiller 1961; Savage 1977; Hakim *et al.* 1990; Coyle 1992; Gurfinkel Castillo 1995). However, surface tension, acting through both 'in plane' and spanwise curvature, will oppose this growth; hence the capillary number as the critical parameter governing the instability.

1.2. *Objectives*

Despite the agreement between linear stability analysis (Coyle *et al.* 1990*b*; Rabaud *et al.* 1991) and experimental observations of the onset of ribbing, several important issues remain unresolved:

(*a*) Previous work cannot explain experimental observations of ribs over the entire roller surface, or on the web far downstream from the meniscus. The source of the instability outlined above – the free-surface normal pressure gradient – is not present on the rolls; indeed, Coyle *et al.* (1990*b*) report eigenfunctions which decay rapidly (spatially) in the downstream direction. This result indicates that the presence, or more precisely, spatial persistence, of ribs cannot be explained solely in terms of linear stability arguments.

(*b*) Previous work, in particular linear stability theory, cannot address the nonlinear evolution and resulting spatial structure of finite-amplitude ribs. Prediction of the nonlinear amplitude of ribs is critical both to the design of effective coating procedures and to the selection of optimal operating parameters: it is the persistence of ribs of finite amplitude, and not simply the meniscus-local presence of free-surface waviness, that determines the quality of the finished product.

In this paper we propose numerical methods for the study of the nonlinear evolution and spatial structure of ribs in symmetric forward-roll coating flows; we describe a framework for understanding the formation, evolution, and spatial persistence of ribs; and we shed light on the apparent contradictions between previous analytical work and experimental observations. We formulate the problem in §2; present the mechanism for ribbing in §3; discuss our numerical methods in §4; reproduce existing results for two-dimensional forward-roll coating in §5; present new results for three-dimensional finite-amplitude ribs in §6; and briefly state our conclusions in §7.

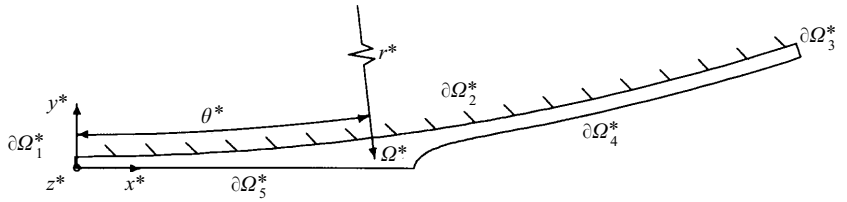

FIGURE 2. Two-dimensional domain Ω^* and associated boundaries: $\partial\Omega_1^*$, inflow; $\partial\Omega_2^*$, roller; $\partial\Omega_3^*$, outflow; $\partial\Omega_4^*$, free surface; and $\partial\Omega_5^*$, symmetry.

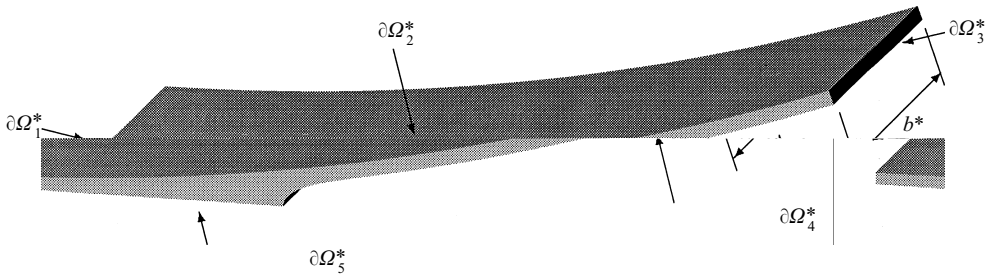

FIGURE 3. Three-dimensional domain Ω^* and associated boundaries: $\partial\Omega_1^*$, inflow; $\partial\Omega_2^*$, roller; $\partial\Omega_3^*$, outflow; $\partial\Omega_4^*$, free surface; and $\partial\Omega_5^*$, symmetry.

2. Problem formulation

The symmetric forward-roll coating device depicted in figure 1 consists of two cylinders of equal diameter D^* separated by a gap H^* counter-rotating at the same angular rate ω^*. In the analysis that follows, we consider a reduced problem on the symmetrized domain, Ω^*, shown in figures 2 and 3 for the two-dimensional and three-dimensional cases, respectively. The domain Ω^* has boundary $\partial\Omega^* = \bigcup_{i=1}^{5} \partial\Omega_i^*$, comprising five parts: $\partial\Omega_1^*$, inflow; $\partial\Omega_2^*$, roller; $\partial\Omega_3^*$, outflow; $\partial\Omega_4^*$, free surface; and $\partial\Omega_5^*$, symmetry. For three-dimensional analyses we limit our considerations to domains that are b^*-periodic in the spanwise (z^*) direction; one periodic cell of the domain is shown in figure 3. A periodic domain of finite length, b^*, does not permit the study of the complete three-dimensional geometry of a forward-roll coating device; in particular, we cannot consider end effects, which might give additional insight into the nature of the ribbing instability (Coyle *et al.* 1990*b*; Rabaud *et al.* 1991; Bruyn & Pan 1995).

The domain extends at inflow up to the point at which the cylinders are closest (Coyle *et al.* 1986) – the nip region – and extends sufficiently downstream of the nip (at outflow) so that the film profile and the pressure become uniform or, at least, change very slowly. Our assumption (like that of Coyle *et al.* 1986, 1990*b*) of symmetry about the $y^* = 0$ plane, $\partial\Omega_5^*$, improves numerical conditioning, decreases the number of degrees of freedom, and reduces the overall computational time; collateral 'full domain' numerical calculations reported by Gurfinkel Castillo (1995) suggest that both the two-dimensional steady states and the nonlinear three-dimensional free-surface evolution are, indeed, y^*-symmetric for the range of Ca studied.

2.1. *Governing equations*

We consider the unsteady incompressible creeping flow of a Newtonian fluid of viscosity μ^* and density ρ^* in the time-dependent domain Ω^*. The non-dimensional

(without superscript *) governing equations are then given by

$$Re\, u_{i,t} = -(p)_{,j}\, \delta_{ij} + \left(u_{i,j} + u_{j,i}\right)_{,j} \qquad \text{in} \quad \Omega, \tag{2.1}$$

with boundary conditions

$$\left.\begin{aligned} n_i \left[-p\, \delta_{ij} + u_{i,j} + u_{j,i}\right] n_j &= p_{nip} \\ t_i \left[u_{i,j} + u_{j,i}\right] n_j &= 0 \end{aligned}\right\} \text{on} \quad \partial\Omega_1, \tag{2.2}$$

$$u_i = V\, t_i \qquad \text{on} \quad \partial\Omega_2, \tag{2.3}$$

$$\left.\begin{aligned} n_i \left[-p\, \delta_{ij} + u_{i,j} + u_{j,i}\right] n_j &= p_{out} \\ t_i \left[u_{i,j} + u_{j,i}\right] n_j &= 0 \end{aligned}\right\} \text{on} \quad \partial\Omega_3, \tag{2.4}$$

$$\left.\begin{aligned} n_i \left[-p\, \delta_{ij} + \left(u_{i,j} + u_{j,i}\right)\right] n_j &= \left(1/Ca\right)\kappa \\ t_i \left[u_{i,j} + u_{j,i}\right] n_j &= 0 \end{aligned}\right\} \text{on} \quad \partial\Omega_4, \tag{2.5}$$

$$\left.\begin{aligned} u_i\, n_i &= 0 \\ t_i \left[u_{i,j} + u_{j,i}\right] n_j &= 0 \end{aligned}\right\} \text{on} \quad \partial\Omega_5, \tag{2.6}$$

and spanwise periodicity for all variables (say ξ) and associated derivatives,

$$\xi\,(x, y, z, t) = \xi\,(x, y, z + b, t) \qquad \text{in} \quad \Omega. \tag{2.7}$$

Finally, the domain Ω is time-dependent: the velocity normal to $\partial\Omega_4$ of a material point on the free surface must coincide with the corresponding fluid normal velocity, $u_k\, n_k|_{\partial\Omega_4}$.

We use standard Cartesian indicial notation (e.g. $u_{i,j} = \partial u_i/\partial x_j$), where subscript indices range from 1 to 2 or 3 for the two-dimensional or three-dimensional problem, respectively; δ_{ij} is the Kronecker-delta symbol; κ is twice the mean curvature; n_i is the unit normal on $\partial\Omega$; t_i is the unit tangent (or tangents) on $\partial\Omega$; p_{nip} and p_{out} are the pressures imposed at inflow and outflow, respectively; σ^* is the surface tension at the fluid free surface; $Re = \rho^* V^* H^*/\mu^*$ is the Reynolds number; $Ca = \mu^* V^*/\sigma^*$ is the capillary number; and $V^* = \omega^* D^*/2$ is the tangential speed of the rollers. In two dimensions, the single tangent satisfies $t_i \times n_i = \hat{z}$; in three dimensions, (2.2), (2.4), (2.5), and (2.6) apply for each tangent, however t_i in (2.3) refers only to the first tangent, assumed to be in the $x \times y$ plane of the roller.

Here length (x_i), velocity (u_i), time (t), and pressure (p) are scaled by H^*, V^*, H^*/V^*, and $\mu^* V^*/H^*$, respectively. Although by definition H and V are equal to unity, they are occasionally explicitly included for clarity. For future reference, we also introduce several auxiliary coordinates: r and h, to measure the radial position; and s and θ, to measure the downstream position along the rollers. The coordinate r (see figure 2) measures the distance to the centre of the roller, $r = (x^2 + (D/2 + H/2 - y)^2)^{1/2}$, while h is the distance to the roller surface, $h = r - D/2$. The coordinate θ (see figure 2) measures position downstream from the nip, $\theta = \arccos\left(x/r\right)$, while the coordinate s measures the arclength parallel to the surface of the roller from the point at which the cylinders are closest, $s = r\,\theta$.

Finally, we consider in more detail the boundary conditions at inflow and outflow. As regards inflow, we make the simplifying assumption that the region upstream of the nip is flooded (Coyle *et al.* 1986), and, in addition, that the flow in this region admits adequate approximation by lubrication theory. The pressure at the nip, p_{nip}, is thus only a function of the total volumetric flow rate per unit depth (Taylor 1963;

Coyle *et al.* 1986),

$$p_{nip} = \tfrac{3}{4}\sqrt{2}\pi \left[1 - \tfrac{3}{4}Q\right] 2\, D^{1/2}, \tag{2.8}$$

where $Q = Q^*/(V^* H^*)$, and Q^* is the total volumetric flow rate per unit depth through the nip. Equation (2.8) must be solved in concert with the fluid flow equations. Note that it is only in (2.8) that lubrication theory enters into our calculations (Reinelt 1995).

Proceeding now to outflow, we note that, sufficiently far downstream of the nip, the film profile and the pressure become uniform. The domain considered extends a finite arclength $s_{\partial\Omega_3}$ along the roller, equivalent to an angle $\theta_{\partial\Omega_3}$; on $\partial\Omega_3$, that is, at $\theta = \theta_{\partial\Omega_3}$, we impose

$$p_{out} = \frac{1}{Ca}\,\frac{2}{D + 1.3\,H}, \tag{2.9}$$

which is an estimate for the pressure jump across the free surface of the uniform downstream film (Gurfinkel Castillo 1995). This boundary condition is asymptotically consistent with (2.1)–(2.6) as $D/H \to \infty$ and $s_{\partial\Omega_3} \to \infty$.

2.2. *Governing parameters*

In the problem formulation above we neglect advection and gravitational terms, since these effects are, first, often not important, and second, not necessary to explain and study the basic mechanisms of ribbing. In particular, we concentrate on flows which commonly exhibit ribbing and in which inertial effects are negligible, $Re \to 0$ (and hence $ReCa \to 0$ for fixed Ca), as is typically the case in configurations that involve extremely viscous fluids (e.g. $H^* = 100\,\mu\text{m}$, $D^* = 0.2$ m, $\mu^* = 11$ Pa s, $\rho^* = 1000$ Kg m^{-3}, $\sigma^* = 0.4$ N m^{-1}, and $V^* = 0.12$ m s^{-1} yields $Re = 1 \times 10^{-2}$, see Coyle 1992). This allows us to neglect the advection term, $Re\, u_j\, u_{i,j}$, in the Navier–Stokes equations in arriving at (2.1). We do not, however, eliminate the unsteady term, $Re\, u_{i,t}$, since the time constant associated with evolution of the instability is not known *a priori*. As will be seen in §6, the time constant is such that the temporal dependence of the problem enters primarily through the deformation of the physical domain; thus, *a posteriori*, the $Re\, u_{i,t}$ term can be safely discarded, yielding a quasi-steady Stokes problem in a time-dependent domain.

The ratio of gravitational forces to viscous forces, given by the Stokes number $St = \rho^* g^* (H^*)^2/(\mu^* V^*)$, and the ratio of gravitational forces to surface tension forces, given by the Bond number $Bo = St\,Ca = \rho^* g^* (H^*)^2/\sigma^*$, are also assumed small in this investigation and thus, by construction, we need not include gravity effects (here g^* is the acceleration due to gravity). Neglecting gravitational and inertial effects places restrictions on the gap H^* and the tangential velocity V^*: in particular, we cannot consider flows in the 'wide-gap regime', in which Re, St, and Bo are order unity (Canedo & Denson 1989; Wang & Domoto 1994). Note also that we cannot accurately treat 'start-up' flows from rest, as gravity will clearly predominate for short times.

Within the stated assumptions, the physical problem is thus governed by three parameters:

$$D = \frac{D^*}{H^*}, \tag{2.10}$$

$$Ca = \frac{\mu^* V^*}{\sigma^*}, \tag{2.11}$$

$$b = \frac{b^*}{H^*}, \tag{2.12}$$

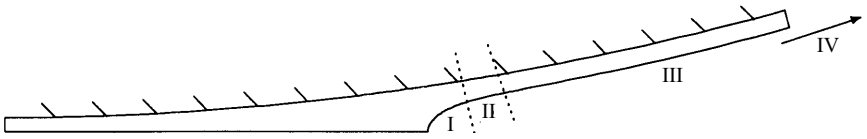

FIGURE 4. Schematic showing regions of ribbing flow geometry and flow field: I meniscus; II transition; III levelling film; IV levelled film.

where D is a geometric quantity that measures the relative importance of roller curvature to roller separation, Ca is the ratio of viscous forces to surface tension forces, and b is the spanwise 'box size'. For the two-dimensional problem, only D and Ca are of interest. Values of D and Ca in actual manufacturing processes can span several orders of magnitude, $D \in [50, 50\,000]$ and $Ca \in \left[10^{-3}, 10^{3}\right]$; we will only consider those (intermediate) values of D and Ca for which steady ribs can be readily observed. We will, however, study a range of box sizes b. Note that in considering a specific value of b, we impose a lower bound on the possible wavenumber content, that is, we admit only wavenumbers $\beta = m\pi/b$ for $m = 1, \ldots, \infty$.

3. Nonlinear framework for ribbing

In this section we present a framework for understanding ribbing in terms of two well-understood physical phenomena: the growth of disturbances on a splitting meniscus (Pearson 1960; Pitts & Greiller 1961; Savage 1977; Ruschak 1985; Coyle *et al.* 1990*b*; Rabaud *et al.* 1991), and the levelling of a viscous film under the effects of surface tension (Levich 1962; Orchard 1962; Kheshgi 1989; Probstein 1995). Since the flow fields of these two phenomena are not compatible, we match the two regimes by means of a transition region. In total, we describe the ribbed free-surface geometry and flow field by the four regions shown in figure 4. A brief summary of each region follows:

I Meniscus: In this region the pressure gradient normal to the free surface is sufficiently large for ribs to grow and develop. The flow field is 'diverging' in nature: the fluid near the free surface moves toward the crests of the ribs and away from the troughs.

II Transition: In this region the flow field of the meniscus is matched to that of a levelling film. The pressure gradient is not great enough to sustain the diverging flow field, which decays due to the effects of viscosity towards the levelling solution. The transition-region length is of order unity: $L_t = L_t^*/H^* \approx O(1)$.

III Levelling film: In this region there is no appreciable pressure gradient, and thus the ribs level under the effect of surface tension. This region can be extremely long, depending on the wavenumber content and amplitude of the rib disturbance created at the meniscus.

IV Levelled film: In this region the film is rib-free and the flow field is one-dimensional.

In what follows, we address the mechanisms associated with the model in more detail: first we discuss the nonlinear nature of ribbing (I); next we evoke film levelling to explain the spatial persistence of ribs (III); finally, we match these two regimes (II) to construct the complete model. The discussion that follows is only relevant for flows for which ribbing is observed. It will become clear that certain quantitative aspects of our model are incomplete, and must be provided by our full numerical computations.

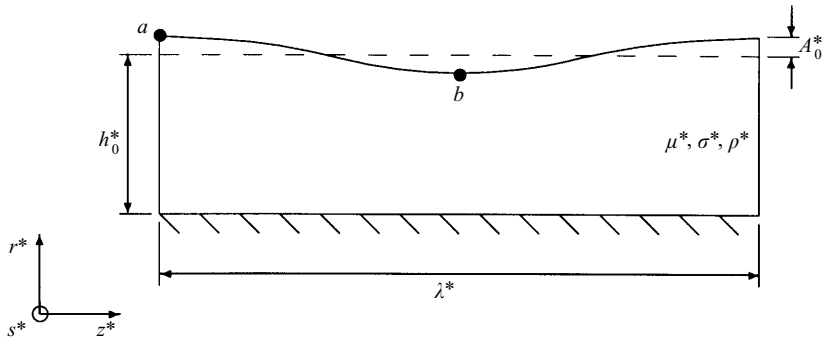

FIGURE 5. Levelling of a thin viscous film. The flow is in the (r^*, z^*)-plane (r^* is normal to the surface of the roller), driven by surface-tension-induced pressure gradients in the z^*-direction.

3.1. *Meniscus instability*

As described in §1, for sufficiently large Ca, the two-dimensional solutions are unstable to spanwise perturbations to the free surface for wavenumbers $\beta \in [\beta_L, \beta_H]$. As a result of this supercritical bifurcation, an initially small disturbance will evolve into a finite-amplitude rib, the amplitude and structure of which we present (based on numerical results) in §6.

The driving pressure gradient normal to the free surface becomes vanishingly small outside the meniscus region, and ribs, therefore, cannot grow either in the transition region or further downstream. This observation is supported by the rapidly decaying eigenfunctions found in the linear stability analysis of Coyle *et al.* (1990*b*); this picture is also consistent with the experimental observations of Hasegawa & Sorimachi (1993), in which local quenching of the instability in the meniscus region eliminates ribbing everywhere downstream. Based on these arguments, we conclude that ribs observed downstream of the meniscus can only originate in the meniscus.

3.2. *Levelling of viscous films*

In order to understand the spatial persistence of ribs, we first look at the physics of levelling. We consider the levelling of a fluid film of mean thickness h_o^* and viscosity μ^* under the effect of surface tension σ^* (Orchard 1962; Kheshgi 1989). At time $t = 0$ the free-surface disturbance is of sinusoidal shape of amplitude A_0^* and wavelength λ^*, as depicted in figure 5. We first consider the film to be infinite and invariant in s^*, and subsequently include the 'roller-propagated' spatial decay.

We restrict our attention, as before, to configurations for which gravity and fluid inertia terms are unimportant. If we assume that the perturbation amplitude is small compared to the wavelength, $A^* \ll \lambda^*$, and that the wavelength is large compared to the film thickness, $\lambda^* \gg h_o^*$, the pressure difference that drives the levelling of the film scales as $\Delta p^* \approx p_a^* - p_b^* \approx \sigma^* A^*/(\lambda^*)^2$, and thus $\Delta p^*/\Delta z^* \approx \sigma^* A^*/(\lambda^*)^3$. Assuming locally fully developed plane Poiseuille flow, the local volume flow rate (per unit s^* depth) in the spanwise direction is then given by $Q_z^* \approx (1/\mu^*)\,(\Delta p^*/\Delta z^*)\,(h_o^*)^3$. As the volume of fluid that must be displaced scales with $\lambda^* A^*$, the time to equilibration scales as

$$\tau^* \approx \frac{\lambda^* A^*}{Q_z^*} \approx \frac{\mu^*}{\sigma^*} h_o^* \left(\frac{\lambda^*}{h_o^*}\right)^4 \quad \left(\text{for} \quad \frac{\lambda^*}{h_o^*} \gg 1\right). \tag{3.1}$$

It can also be shown (Orchard 1962; Kheshgi 1989; Gurfinkel Castillo 1995) that, in the limit of short-wavelength disturbances, the time to level scales linearly with the

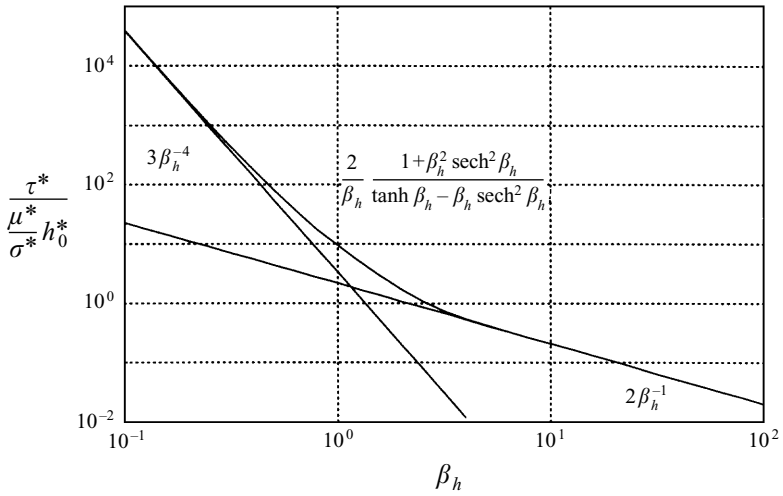

FIGURE 6. Time constant associated with the levelling of a disturbance on a thin film as a function of the wavenumber $\beta_h = 2\pi h_0^*/\lambda^*$.

wavelength of the disturbance,

$$\tau^* \approx \frac{\mu^*}{\sigma^*} h_o^* \left(\frac{\lambda^*}{h_o^*}\right) \quad \text{for} \quad \frac{\lambda^*}{h_o^*} \ll 1. \tag{3.2}$$

Orchard (1962) and Kheshgi (1989) solve the equations of motion exactly for small-amplitude disturbances without restrictions on the wavelength; the expression for the timescale associated with levelling is shown to be

$$\tau^* = 2\frac{\mu^*}{\sigma^*} h_o^* \frac{1}{\beta_h} \frac{1+\beta_h^2\,\mathrm{sech}^2\beta_h}{\tanh\beta_h - \beta_h\,\mathrm{sech}^2\beta_h}, \tag{3.3}$$

where β_h is the non-dimensional wavenumber based on the average film thickness, $\beta_h = 2\pi h_o^*/\lambda^*$. Here τ^* is defined such that the evolution of the amplitude of the disturbance is given by $A^*(t^*) = A_0^* \exp\left(-t^*/\tau^*\right)$. Equation (3.3) reduces to the functional forms of (3.1) and (3.2) in the appropriate limits, as shown in figure 6. Recall that, to obtain (3.3), we neglect gravitational effects which would accelerate levelling, in particular for longer wavelength ribs; gravity thus sets a low-wavenumber cutoff for the ribbed geometries that can be described accurately by this analysis.

To consider the movement of a fluid film entrained by rollers, we must now superimpose on the levelling solution a velocity V^* normal to the plane of the film. Levelling can be interpreted to occur as the film moves in the downstream direction; time in (3.1), (3.2), and (3.3), can then be replaced by the distance travelled downstream, s^*, divided by the superimposed velocity, V^*. From the previous expressions, the length scale in the downstream direction associated with levelling, $L_\ell = L_\ell^*/H^*$, can be estimated as

$$L_\ell = 3\,Ca\,\beta_{h_{\mathrm{IV}}}^{-4} h_{\mathrm{IV}} \quad \text{for} \quad \frac{\lambda}{H} \gg 1, \tag{3.4}$$

$$L_\ell = 2\,Ca\,\beta_{h_{\mathrm{IV}}}^{-1} h_{\mathrm{IV}} \quad \text{for} \quad \frac{\lambda}{H} \ll 1, \tag{3.5}$$

where h_{IV} $(= h_{\mathrm{IV}}^*/H^*)$ is the levelled film thickness, readily calculable once Q, the volume flow rate per unit depth, is known. (A value of $Q \approx 1.3$ can be used as

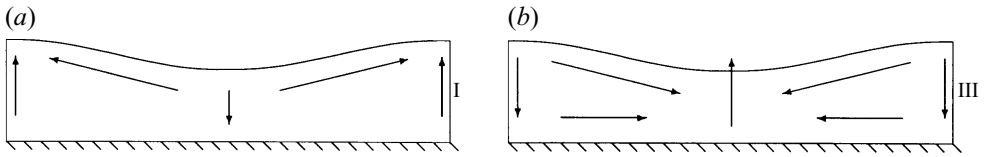

FIGURE 7. Schematic of flow fields: (*a*) meniscus region, (*b*) levelling region.

an estimate in forward-roll coating, as seen in §5.) Here L_ℓ is defined such that the film amplitude decays as $\exp\left(-s/L_\ell\right)$, where s is the distance along the roller; the temporal-to-spatial transformation formally requires that $L_\ell \beta_h$ be sufficiently large.

Equations (3.3), (3.4), and (3.5) show two characteristics of levelling that we will need to explain the spatial persistence of ribs. First, increased viscosity hinders the levelling process, in effect decreasing the damping of the free-surface perturbation. Second, the distance over which levelling takes place, L_ℓ, decreases monotonically with wavenumber: high-wavenumber components will decay at a faster rate than low-wavenumber components.

3.3. *Transition from ribbing to levelling*

The two flow fields discussed – meniscus and levelling – do not match; in the meniscus region, the fluid is drawn into the crests of the ribs and away from the troughs, as shown schematically in figure 7(*a*), while in levelling films, fluid is drained from the crests, as shown schematically in figure 7(*b*). The flow geometries and flow fields are matched in what we term the transition region. It can be shown, based on a separation-of-variables argument (Gurfinkel Castillo 1995), that the diverging velocity field will decay under the action of viscosity over a length, $L_t = L_t^*/H^*$, which is on the order of the film thickness, $h_{\mathrm{IV}} = h_{\mathrm{IV}}^*/H^*$. In fact, this assumes that the downstream pressure gradient is zero in the transition region; in reality, the pressure gradient is not identically zero, just not large enough to support the ribs, and thus the meniscus velocity profiles decay over a slightly larger distance. On leaving the transition region, the ribs level following the mechanisms outlined above.

3.4. *Summary*

The pressure gradient caused by in-plane curvature in the meniscus region (I) generates ribs that move downstream with the rollers. As the ribs proceed downstream, the flow field under the ribs suffers a (spatial) transition (in region II), over a distance of order h_{IV}, from the helical nature of the meniscus region to the 'convergent' flow field of the levelling film region. Upon leaving the transition region, the ribs begin levelling and persist downstream over a very long distance (region III), the extent of which is given by (3.4) and (3.5). Owing to the dependence of the levelling rate on the wavenumber content of the rib profile, the rib profile first becomes monochromatic (still in the levelling region III) and, eventually, uniform far downstream (in region IV).

We now present the numerical methods and the numerical calculations by which we verify and quantify these predictions: the instability of the meniscus and subsequent growth and saturation of meniscus ribbing; the coupling between the instability of the meniscus and the ribs observed downstream; the rapid change in the spanwise flow field in the transition region; and the slow levelling of the ribs.

4. Numerical methods

In this section, we first present the methods used to generate the two-dimensional base states required as a point of departure for our three-dimensional simulations. We then present the methods used to obtain the three-dimensional steady ribbed states. In each subsection we summarize the numerical methods adopted, discuss the treatment of any non-conventional boundary conditions, and present the remeshing and continuation algorithms developed. The numerical methods described in §§4.1.1 and 4.2.1 are implemented in a commercial fluid-dynamics code, NEKTON^{TM}. In particular, the commercial code serves as the simulation engine around which we build our problem-specific algorithms for boundary conditions, remeshing, and continuation (Gurfinkel Castillo 1995).

4.1. *Methods for two-dimensional flows*

4.1.1. *Discretization and solution*

For the solution of steady ($u_{i,t} \equiv 0$ in (2.1)) two-dimensional problems, NEKTON^{TM} follows the numerical procedure developed by Ho & Rønquist (1992) for the efficient treatment of flows in which surface tension forces play an important role in determining free-surface geometry. A brief description of the solution algorithm, hereafter referred to as S, follows:

S0 Initialize iteration counter, $S_I = 0$.

S1 Solve the spectral element spatial discretization of (2.1) subject to $u_i n_i = 0$ and $t_i \left[u_{i,j} + u_{j,i}\right] n_i = 0$ on the free surface, $\partial\Omega_4$, with the remaining boundary conditions on $\partial\Omega \setminus \partial\Omega_4$ as described by (2.2), (2.3), (2.4), and (2.6).

S2 Compute the residual traction on $\partial\Omega_4$ based on the solution of step S1. The residual traction is defined as $r_i \equiv \tau_{ij} n_j - \sigma \kappa n_i$, in which $\tau_{ij} n_j$ is the traction on the free surface; r_i is identically zero for a steady-state solution.

S3 Perform direct solution of a Poisson problem for the correction to the free-surface geometry, Δx_i. In particular, the correction to the free-surface curvature is expressed as a function of Δx_i, yielding a Poisson problem in which the residual traction, r_i, enters as the inhomogeneity.

S4 Extend Δx_i, slightly under-relaxed, into the interior of the domain by means of an elliptic (partial-differential-equation) operator (Ho & Patera 1990).

S5 Update all the mesh coordinates and the iteration counter, $S_I = S_I + 1$.

Steps S1 to S5 are repeated until the maximum Δx_i over all free-surface nodes is 1.5×10^{-4}; when this tolerance is met, the flow is taken to be sufficiently close to a steady state. Tolerances based on iteration-matrix minimum eigenvalues or condition number would be preferred, but are not yet implemented.

The essential ingredients of this numerical procedure are: variational description of the curvature (Ruschak 1980; Ho & Patera 1990); spectral element spatial discretization (Rønquist 1988; Maday & Patera 1989); decoupled treatment of the domain geometry; solution of the nonlinear system of discretized momentum equations by Newton–Raphson iteration; and direct serial solution of the free-surface curvature correction (Ho & Rønquist 1992). The variational description of the curvature provides a surface-intrinsic natural (weak) condition for continuity of the surface tangent across elemental boundaries, and does not require a global coordinate system, orthogonal local coordinate systems, or a C^1 free-surface description; the spectral element spatial discretization provides a high-order representation of both the fluid flow and flow geometry, and requires, for sufficiently regular solutions and stringent accuracy requirements, fewer degrees of freedom and less computational effort than a low-order

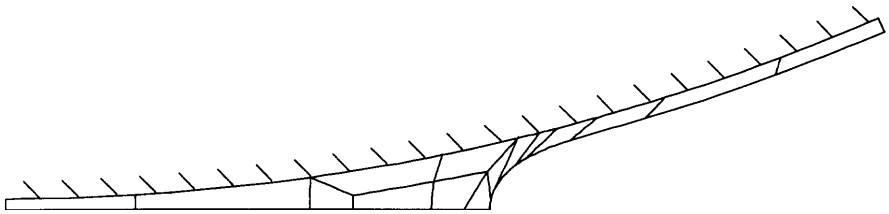

FIGURE 8. Example of a greatly distorted (vanishing Jacobian) mesh that arises during the non-remeshed solution procedure S for $D = 200$, $Ca = 1$.

approach; and the decoupled treatment of the domain geometry and the flow solution reduces the problem size relative to a coupled treatment, and permits fast subproblem solution strategies. Note the spectral element domain discretization also allows for simpler remeshing techniques due to the local structure intrinsic to the mesh.

4.1.2. *Treatment of inflow boundary condition*

As described in the problem formulation, the boundary condition at inflow, $\partial\Omega_1$, relates the pressure at the nip, p_{nip}, to the volume flow rate per unit depth through the nip, Q; the latter, however, is not known *a priori*. Equation (2.8) is solved with the fluid flow equations by means of an outer iteration, OI; this is possible since the dependence of the final flow geometry on the nip pressure is weak. The treatment is as follows:

OI0 Assume a value of $Q = Q_0 = 1.3$ to calculate the corresponding pressure at the nip, p_{nip}, based on (2.8). Initialize the outer iteration counter, $\mathrm{OI_I} = 1$.

OI1 Solve for the steady-state geometry, flow field, and hence flow rate $Q_{\mathrm{OI_I}}$, using the procedure S described above.

OI2 Recompute the pressure at the nip from (2.8) based on a new volume flow rate

$$Q = \frac{Q_{\mathrm{OI_I}} + K_{\mathrm{OI}}\, Q_{\mathrm{OI_I}-1}}{1 + K_{\mathrm{OI}}}, \tag{4.1}$$

and update the outer iteration counter $\mathrm{OI_I}$. The under-relaxation constant K_{OI} is conservatively set to 6; smaller values can be used for $Ca > 1$, as for these cases the flow rate is only weakly dependent on Ca.

If steps OI1 and OI2 are repeated until there is no appreciable change in the computed steady flow geometries – say, using a stopping criterion based on the maximum change of position over all free-surface mesh nodes between two computed steady states, $\max_{\partial\Omega_4} \Delta x_i < 1 \times 10^{-4}$ – incorrect flow rates are obtained, as (2.8) will not be satisfied. This is because the flow rate is a measure of the overall meniscus shape, not the 'local' meniscus position, and thus small local changes in the meniscus geometry can yield very different flow rates. We thus adopt a stopping criterion that, in addition to $\max_{\partial\Omega_4} \Delta x_i < 1 \times 10^{-4}$, requires that the difference in the flow rate between two computed steady states be less than 0.05%.

4.1.3. *Remeshing of two-dimensional geometries*

For very large surface deformations the elliptic partial-differential-equation extension scheme for the mesh coordinates (Ho 1989; Ho & Patera 1990) may yield elements that are nearly singular, that is, exhibit vanishing Jacobians, as observed in figure 8. To remedy this problem we initiate automatic remeshing procedures (Gurfinkel Castillo 1995) when the iteration counter $\mathrm{S_I}$ exceeds a given value. A new spectral element mesh is constructed based on (i) a series of templates (e.g. figures

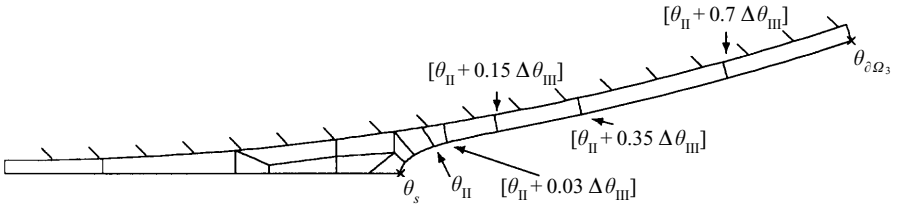

FIGURE 9. Representative information in mesh template for a two-dimensional domain discretization.

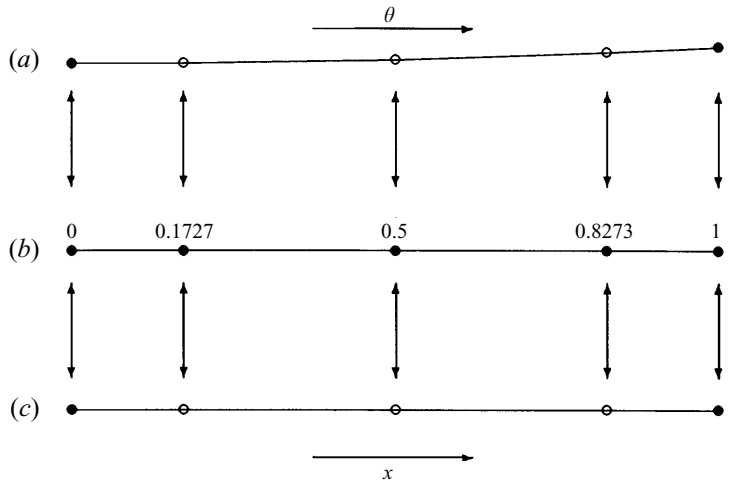

FIGURE 10. Example of a fourth-order-interpolant edge template for the position of element-edge internal nodes given edge boundary nodes: (*a*) nodes on rollers or free surface, (*b*) edge template with Gauss–Legendre–Lobatto spacing, and (*c*) nodes on the mid-plane.

9 and 10), which provide the topology and relative placement of the elements and nodes, and (ii) the current mesh, which provides the geometry, and, in particular, the position of the meniscus. The remeshing procedure, R, is as follows:

R1 Extract necessary information from the current mesh: the position, x_s^{2D} and θ_s, of the mesh node where the free surface meets the symmetry plane; the piecewise polynomials that define the free surface $\partial\Omega_4$; and the film thickness at outflow, $h_f\left(\theta_{\partial\Omega_3}\right)$.

R2 Compute the desired position of the outflow boundary $\partial\Omega_3$, $\theta_{\partial\Omega_3} = 2\,\theta_s$, and an estimate for the position of the end of the meniscus region, $\theta_{II} = \theta_s + 0.8\,\pi/180$. The meniscus region length is thus $\Delta\theta_{II} = \theta_{II} - \theta_s$ and the film angular extent is $\Delta\theta_{III} = \theta_{\partial\Omega_3} - \theta_{II}$.

R3 Position element-edge boundary (vertex) nodes on the rollers $\partial\Omega_2$ and on the mid-plane $\partial\Omega_5$ following the template description shown in figure 9. The element-edge internal nodes are then placed relative to the position of the element-edge boundary nodes by interpolation in arclength using templates such as that shown in figure 10(*b*).

R4 Discretize the free surface in curved segments following the template angular prescription. The mesh nodes are then positioned along the free surface based on the high-order polynomial information extracted in step R1. The variable used to

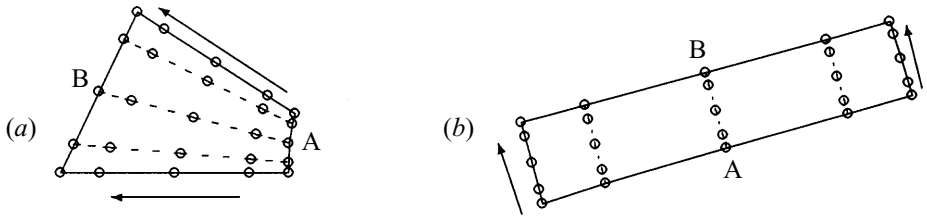

FIGURE 11. Blending algorithm of the two-dimensional remeshing procedure for the position of the internal mesh nodes (step R6). Interpolation is shown for: (*a*) near-quadrangular element, and (*b*) high-aspect-ratio element.

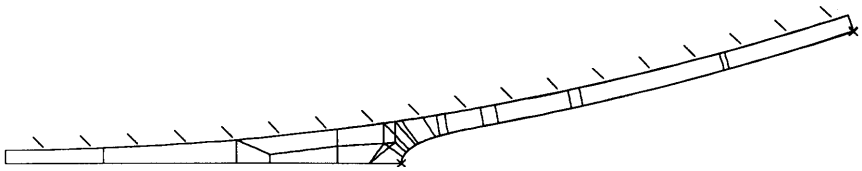

FIGURE 12. Example of remeshing for a not overly deformed domain. The original and final meshes are overlaid.

parameterize the free surface is

$$\tilde{\theta} = \begin{cases} \theta & \text{for} \quad \theta \geqslant \theta_{\mathrm{II}} \\ \arctan\left(\dfrac{y}{\frac{1}{2}(D+H)\tan\theta_{\mathrm{II}} - x}\right)\dfrac{\theta_{\mathrm{II}}}{\frac{1}{2}\pi - \theta_{\mathrm{II}}} & \text{for} \quad \theta < \theta_{\mathrm{II}}, \end{cases} \tag{4.2}$$

which is a continuous single-valued parametrization that satisfies $\tilde{\theta} = 0$ where the free surface intersects the mid-plane. The element-edge internal nodes are placed by interpolation using $\tilde{\theta}$ and the corresponding edge template. Note that, if the outflow is moved away from the nip, information is not available to position the new nodes; for all the mesh nodes in this region, the film thickness is set to be $h_f\left(\theta_{\partial\Omega_3}\right)$, independent of θ.

R5 Construct the remaining internal element edges, as well as the element edges at inflow, $\partial\Omega_1$, and outflow, $\partial\Omega_3$, as straight segments, using the Legendre edge templates to position the nodes.

R6 Position intra-element nodes by interpolation of the positions of element boundary nodes, as shown in figure 11. The particular blending algorithm chosen depends on the aspect ratio of the element under consideration and the shape of the element boundary (Gurfinkel Castillo 1995). A Legendre spacing is preserved on straight lines connecting corresponding nodes on the generating sides (A and B of figure 11).

R7 Map field quantities onto the new mesh. This step is not needed (or used) for the direct-solution creeping-flow two-dimensional problem, but will prove useful later in the time-iterative solution of the three-dimensional problem. A bilinear interpolation scheme is used to compute the field values on the new mesh from the field values of the old mesh. Spectral accuracy is lost in the bilinear interpolation, but subsequently regained at steady state.

An example of the results of a remeshing procedure is shown in figure 12 for a discretization with 15 spectral elements. The order of the interpolant in each direction in each element is 5, resulting in approximately 1500 total degrees of freedom (velocity,

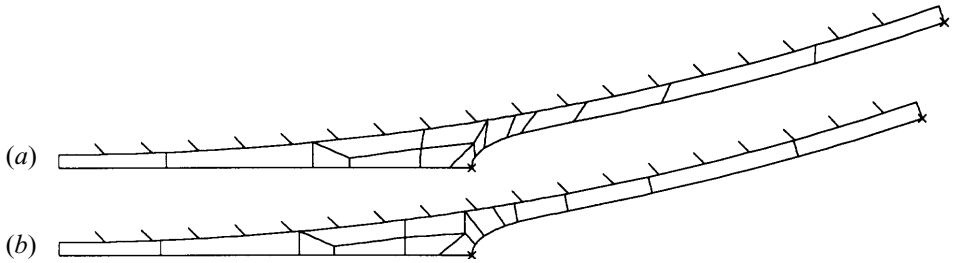

FIGURE 13. Remeshing of greatly distorted elements: (*a*) original mesh, (*b*) new mesh.

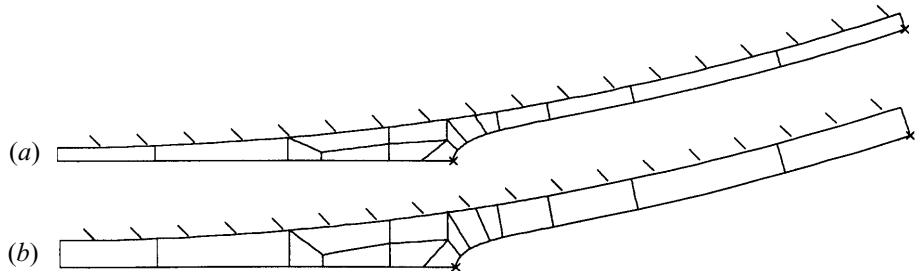

FIGURE 14. Example of remeshing-continuation: change in roller separation from (*a*) $D = 200$ to (*b*) $D = 100$.

pressure, and geometry unknowns). The computational cost associated with this two-dimensional remeshing is small compared to the fluid flow solution, and thus remeshing can be performed every few iterations (S_I), as shown in figure 12, even if not strictly required. If remeshing is performed only when the mesh elements are greatly distorted, the effects of remeshing are more easily visualized, as shown in figure 13.

The modular nature of the remeshing procedure also allows for the implementation of simple continuation schemes in parameter space. For example, if the solution for a new $\{Ca, D\}$ pair is desired, the existing solution for a different geometry D (and Ca) can be modified to construct an initial estimate for the desired solution; more precisely, the nodes on the rollers are moved in the radial direction to the desired gap during step R3 of the remeshing procedure, and the spatial coordinates are then appropriately rescaled. An example of remeshing used for continuation in D is shown in figure 14.

4.2. *Methods for three-dimensional flows*

4.2.1. *Discretization and solution*

The numerical methods used for the simulation of the unsteady three-dimensional free-surface fluid-flow problem comprise: variational description of the curvature in three space dimensions (Ho & Patera 1991); arbitrary-Lagrangian–Eulerian description of the time-dependent domain (Donea 1983; Ho & Patera 1990); spectral element spatial discretization (Rønquist 1988; Maday & Patera 1989; Ho & Patera 1990); semi-implicit fractional time stepping (Ho & Patera 1990; Rønquist 1991); and parallel solution of the implicit (pressure and viscous) operators (Fischer & Patera 1991, 1994) by a preconditioned conjugate gradient algorithm (Rønquist 1991).

As described previously, the variational description of the curvature provides a surface-intrinsic natural (weak) condition for continuity of the surface tangent across

elemental boundaries, and does not require a global coordinate system, orthogonal local coordinate systems, or a C^1 free-surface description. The spectral element spatial discretization allows for simplified domain decomposition and a high-order representation of both the fluid flow and flow geometry – although it should be clear that finite element spatial discretizations would serve equally well. The semi-implicit approach allows for the implicit treatment of those components of the governing equations that admit fast iterative solution via preconditioned conjugate gradient iteration (to wit, the Stokes problem, which is further implicitly split into viscous and pressure substeps), while permitting explicit treatment of those terms not readily amenable to fast iterative solution (in our case the free-surface kinematic condition and geometry-evolution operator).

A drawback to our approach is that explicit treatment of the domain evolution places a stability restriction on the maximum allowable timestep (Ho 1989; Ho & Patera 1990). The timestep criterion proposed by Ho (1989) is too restrictive for the creeping flows ($Re \ll 1$) considered here; we find that, for most of the three-dimensional cases considered in this paper, the timestep can be increased by a factor of 10 over this previous estimate without loss of stability. Nevertheless, simulation of the evolution from the unstable two-dimensional steady states to stable three-dimensional steady ribbed states may require a great number of timesteps, as many as 10^5 in some cases. Note also that our time-stepping scheme will evolve only to stable equilibria.

4.2.2. *Treatment of inflow and outflow boundary conditions*

The treatment of (2.8), the boundary condition at inflow, is similar to the two-dimensional case; in effect, we assume that the total volumetric flow rate, Q, is not greatly affected by the downstream appearance of ribs (Coyle *et al.* 1990*b*). More precisely, if we impose the nip pressure found in the two-dimensional calculation on the three-dimensional flow, the resulting three-dimensional flow rate typically differs from the two-dimensional flow rate by no more than 1%; no iterations are performed to improve this result further.

The boundary condition at outflow, however, presents several difficulties: in three space dimensions, the uniform pressure condition imposed in the two-dimensional case, (2.4), is no longer stable – a spanwise perturbation to the free surface near the outflow will grow (Gurfinkel Castillo 1995). For lack of a better approach, we impose the Draconian – but stable – condition that the free-surface thickness at outflow, $h_f^{3D}(z, \theta_{\partial\Omega_3})$, is uniform in z and equal to the $(D \to \infty)$ two-dimensional levelled film thickness, h_{IV}: we set $h_f^{3D}(z, \theta_{\partial\Omega_3}) = h_{IV}$ for $z \in [0, b]$. The deleterious effect of this boundary condition is limited to a small region (in fact, one spectral element) upstream of the outflow boundary, that is, the free surface transforms from the possibly ribbed geometry to the uniform geometry in the last spectral element in the domain. This perturbation in geometry is accompanied by a perturbation in the spanwise velocity profile which can extend to the second spectral element upstream of outflow in cases in which ribs are of large amplitude near outflow.

4.2.3. *Remeshing of three-dimensional geometries*

A typical discretization of the three-dimensional domain is shown in figure 15. The three-dimensional mesh is an 'extruded' two-dimensional mesh with several levels of elements in the extrusion direction, z. This particular mesh has 4 levels, 60 spectral elements, and elemental interpolants of order 5 (in each spatial direction), resulting in approximately 50 000 degrees of freedom (velocity, pressure, and geometry unknowns).

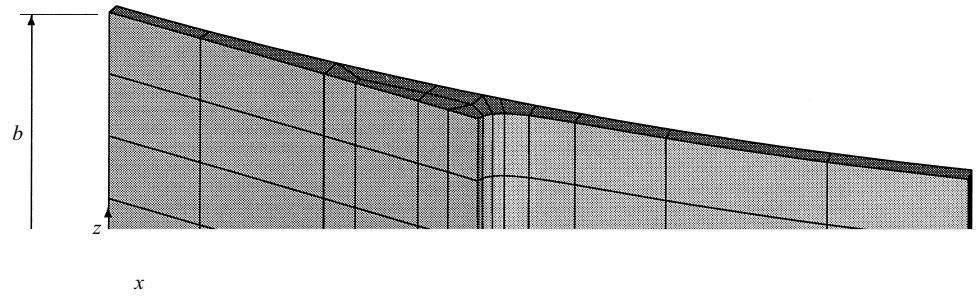

FIGURE 15. Typical three-dimensional discretization of an extruded two-dimensional domain comprising sixty spectral elements arranged in four levels.

To identify the discretization of the domain, we use the triad {number of elements per z level, number of levels, order of the interpolant}, which, for figure 15, is $\{15, 4, 5\}$.

The arbitrary-Lagrangian–Eulerian description of the time-dependent three-dimensional domain avoids frequent remeshing, which, in the three-dimensional case, is rather expensive. However, global remeshing procedures become necessary when the free surface deforms greatly, as can be the case when following the complete evolution from an unstable two-dimensional steady state to a stable three-dimensional steady state. The three-dimensional remeshing procedure is a direct extension of the two-dimensional procedure, but now involves an additional template for the discretization in the z-direction (Gurfinkel Castillo 1995). An overview of the procedure, R^{3D}, follows:

$R1^{3D}$ Extract necessary information from the current three-dimensional mesh: the piecewise polynomials that define $\partial\Omega_4 \bigcap \partial\Omega_5$; the positions, $\left(x_s^{3D}, z_s^{3D}\right)$, of the mesh nodes on $\partial\Omega_4 \bigcap \partial\Omega_5$; and the position, $\left(x_c^{3D}, z_c^{3D}\right)$, of the mesh node on $\partial\Omega_4 \bigcap \partial\Omega_5$ with $z < b/2$ at which the curvature changes sign. We then calculate from this information a measure of the relative steepness of the ribs,

$$\Delta\tilde{z}^{3D} = 2\,\frac{\left|\arg\max_{z_s^{3D}\in[0,b]} x_s^{3D}\left(z_s^{3D}\right) - z_c^{3D}\right|}{b}. \tag{4.3}$$

We shall use this information later to determine the relative sizes of elements in the spanwise direction.

$R2^{3D}$ Calculate, based on $\Delta\tilde{z}^{3D}$ and a spanwise template such as that shown in figure 16, the relative sizes, $\Delta\tilde{z}_i$, of the elements in the spanwise direction; note that different templates are used for different numbers of spanwise levels. The template determines the z-position of the element boundary sides normal to the extrusion direction; the z-position of the corresponding internal nodes is determined using an edge template. The spanwise resolution can be increased by considering more levels of elements.

$R3^{3D}$ Slice the three-dimensional domain in the nodal z-planes defined in step $R2^{3D}$, and apply the two-dimensional remeshing procedure R to each slice (without changing the position of the outflow boundary). Note that in this step trilinear, not bilinear, interpolation is used. The resolution can be increased either by including

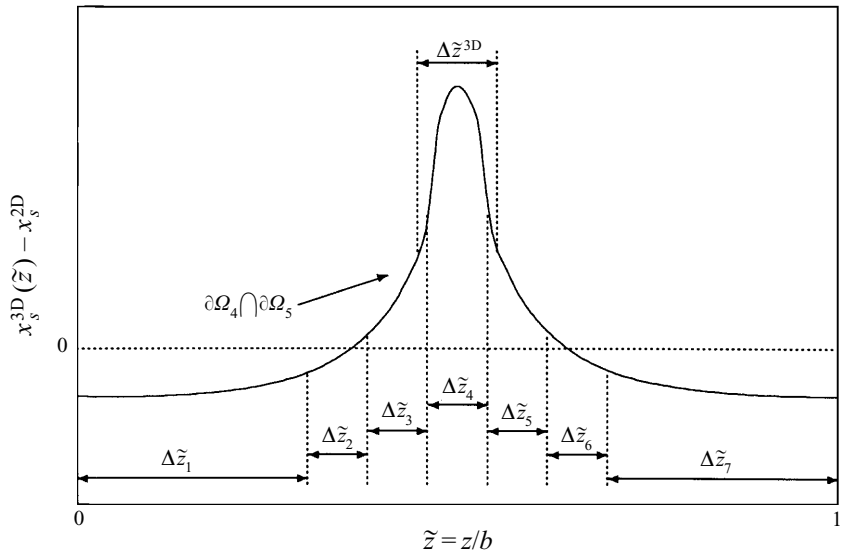

FIGURE 16. Template for the $\tilde{z} = z/b$ coordinate of the element sides normal to the extrusion direction. This template is for a mesh consisting of 7 levels in the spanwise direction.

more elements per level, or by considering higher-order polynomials within each element.

The remeshing procedure R^{3D} does not allow for the study of re-entrant ribs (Tsiveriotis & Brown 1992), as in this case constant z-slices of the three-dimensional domain are no longer topologically equivalent.

4.2.4. *Numerical protocol*

To study the three-dimensional ribbed states, we first obtain the two-dimensional steady flow field. The two-dimensional geometry is then extruded to the desired domain depth b, and the free surface is perturbed sinusoidally with spanwise wavelength b and amplitude A_o^{3D} in the direction of the local free-surface normal. The (non-dimensional) initial amplitude of the perturbation, A_o^{3D}, is taken to be 0.025, except near outflow, where the outflow boundary condition requires $A_o^{3D} \to 0$ as $\theta \to \theta_{\partial\Omega_3}$ (Gurfinkel Castillo 1995). The system of equations (2.1)–(2.8) is then integrated in time according to the numerical procedures described in §4.2.1. As a numerical test, we compare in the Appendix our short-time results for $A_o^{3D} = 5\,10^{-3}$ with the predictions of linear stability theory (Coyle *et al.* 1990*b*); good agreement is obtained.

The steady-state stopping criterion is critical since rib growth can be relatively slow. If the perturbed geometry is integrated in time until the maximum velocity normal to the free surface falls below a preset tolerance, say when $\max_{\partial\Omega_4 \cap \partial\Omega_5} u_i n_i < 0.0025$, the geometry in most cases can be deemed to be close enough to the actual steady state. This criterion fails for slightly supercritical-Ca small-amplitude ribs due to the large time constants ('critical slowing') associated with the rib growth. A tighter stopping criterion is used for such cases, however we have yet to derive a rigorous residual-perturbation relation which reflects the eigenstructure/timescales of the three-dimensional problem.

The computational time to achieve a steady state from the initial two-dimensional perturbed domain depends on the capillary number Ca, the domain depth b, and the resolution $\{.,.,.\}$, but may range from 50 to 800 hours on 16 nodes of an Intel

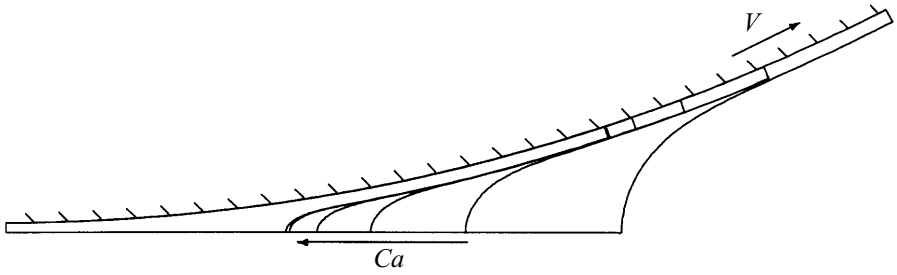

FIGURE 17. Two-dimensional meniscus geometry, for $D = 200$, as a function of capillary number: $Ca = 0.0316, 0.1, 0.316, 1, 3.16, 100$.

i860 Hypercube. The high computational cost is a direct consequence of the explicit treatment of the domain evolution and the resulting restrictive timestep. In order to decrease the computational costs in the future, semi-implicit procedures similar to those used in two dimensions must be pursued.

The spanwise resolution needed to adequately resolve the steady free-surface geometry is not known *a priori*. Initially, when the free surface is not greatly perturbed, relatively few levels of elements suffice; as the free surface deforms, more resolution is required. This increase in resolution is readily effected by selecting a new template, with more levels, in step $R2^{3D}$ of the remeshing procedure R^{3D}. This adaptive resolution scheme can greatly reduce computer time, by as much as an order of magnitude for geometries that require high resolution (e.g. eight levels) in the steady state. Furthermore, once a steady ribbed state is obtained for a given geometry, Ca, and box size, $\{D, Ca, b\}$, continuation and remeshing procedures reduce the computational cost to obtain a new steady ribbed state (e.g. different b) to order 50–200 hours of computer time (Gurfinkel Castillo 1995).

Our numerical procedures also permit relatively inexpensive verification of accuracy. In particular, for certain representative cases, the computed steady ribbed states are mapped onto finer meshes (with more spanwise levels, and higher-order elemental interpolants), and then integrated further in time. No significant changes in meniscus geometry are observed, leading us to conclude that the steady states obtained with the 'coarse' meshes are, indeed, adequately resolved. We also perform a few 'uniform-in-time' higher-resolution simulations from the initial extruded geometry with infinitesimal spanwise perturbation: the same steady solutions are obtained as in the adaptive spanwise-resolution simulations, as will be shown in §6.

5. Two-dimensional results

In this section we first present qualitative results for the two-dimensional problem, and then perform quantitative comparisons with results reported by Coyle *et al.* (1986). Our discussion is brief, intended only as a point of departure for the three-dimensional considerations. Figure 17 shows the dependence of meniscus geometry on the capillary number Ca; with increasing Ca, the meniscus is drawn closer to the nip. This movement is only gradual for high Ca while it is dramatic in the low-Ca range. The downstream migration of the meniscus with decreasing capillary number is accompanied by a qualitative change in the flow field: for low Ca, a recirculation region appears near the meniscus, as shown in figure 18.

We now turn to three quantitative measures of the flow field and geometry: the volume flow rate through the nip, Q; the location of the stagnation point on the

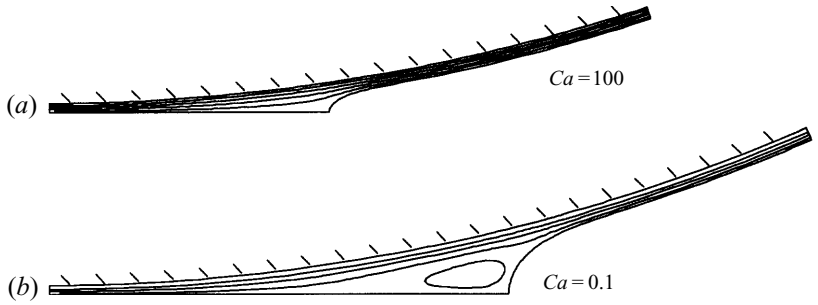

FIGURE 18. Characteristic flow fields (streamlines): (*a*) high Ca – no recirculation zone, (*b*) low Ca – recirculation zone.

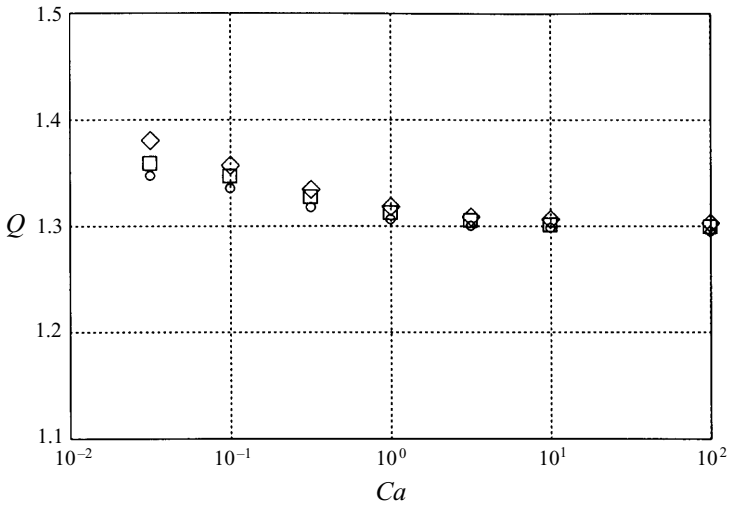

FIGURE 19. Non-dimensional volume flow rate, Q, as a function of Ca for $D = 40$ ($\diamond$), $D = 200$ ($\square$), and$D = 1000$ ($\circ$).

splitting meniscus, x_s^{2D}; and the location of the first stagnation point downstream from the nip along the symmetry plane, x_1^{2D}. The dependence of Q on the capillary number Ca, for $D = 40$, 200 and 1000, is presented in figure 19, which shows the weak dependence of the flow rate, and thus the nip pressure, through (2.8), on the capillary number Ca and on the geometric parameter D. With increasing Ca there is a monotonic decrease in Q. This property is also observed with increasing D, though the dependence it is not as great.

The location of the splitting meniscus is shown in figure 20 as a function of the capillary number Ca for $D = 40$, 200, and 1000. The position of the meniscus, x_s^{2D}, is scaled by the geometric factor $(2D)^{1/2}$ as suggested by lubrication theory analysis (Coyle *et al.* 1986). For most of this parameter range, the $(2D)^{1/2}$ scaling accurately represents the effect of D, however when recirculation sets in at low Ca, the three curves for different D no longer precisely collapse to a single curve.

Figure 21 shows the location of the first stagnation point downstream from the nip along the symmetry plane, x_1^{2D}, as a function of Ca and D. Note that $x_1^{2D} = x_s^{2D}$ ($x_1^{2D} < x_s^{2D}$) in the absence (presence) of recirculation. For high Ca, only one stagnation point is observed along the symmetry plane, $\partial\Omega_5$, that is, there is no

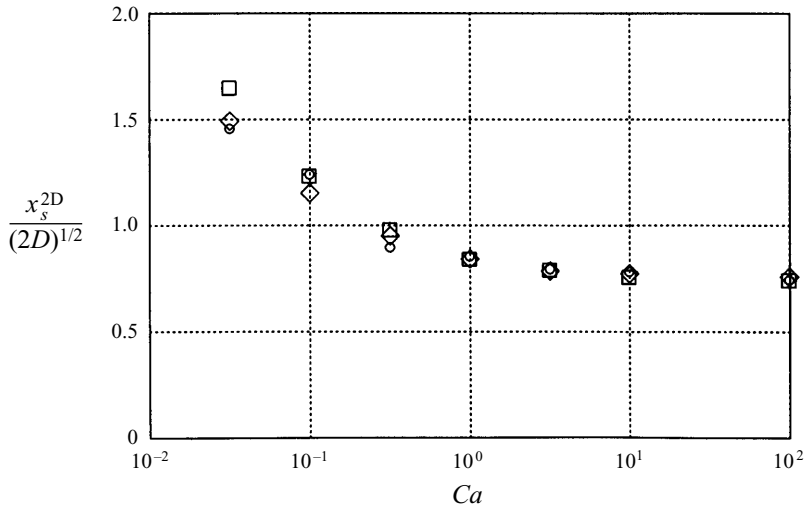

FIGURE 20. Film split location, x_s^{2D}, as a function of $Ca = 0.0316$, 0.1, 0.316, 1, 3.16, 100 for $D = 40$ ($\diamond$), $D = 200$ ($\square$), and $D = 1000$ ($\circ$).

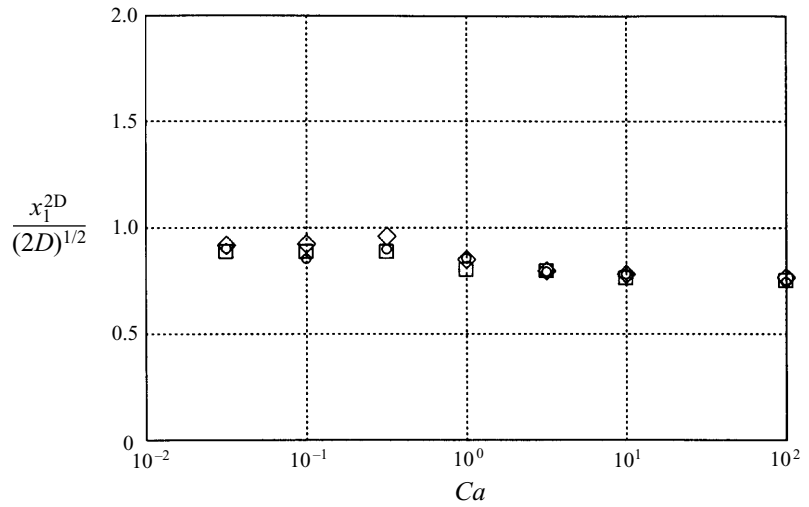

FIGURE 21. Position of first stagnation point downstream from nip, x_1^{2D}, as a function of Ca for $D = 40$ ($\diamond$), $D = 200$ ($\square$),and $D = 1000$ ($\circ$).

recirculation, $x_1^{2D} = x_s^{2D}$. As the capillary number is decreased, near $Ca \sim 0.8$, a second stagnation point arises, $x_1^{2D} < x_s^{2D}$, signalling the presence of a recirculation zone. The location of the first stagnation point downstream of the nip is weakly dependent on Ca, indicating that it is mainly determined by the viscous pressure gradient in the fluid.

Finally, in figure 22, we compare our results with those reported by Coyle *et al.* (1986); excellent agreement is obtained.

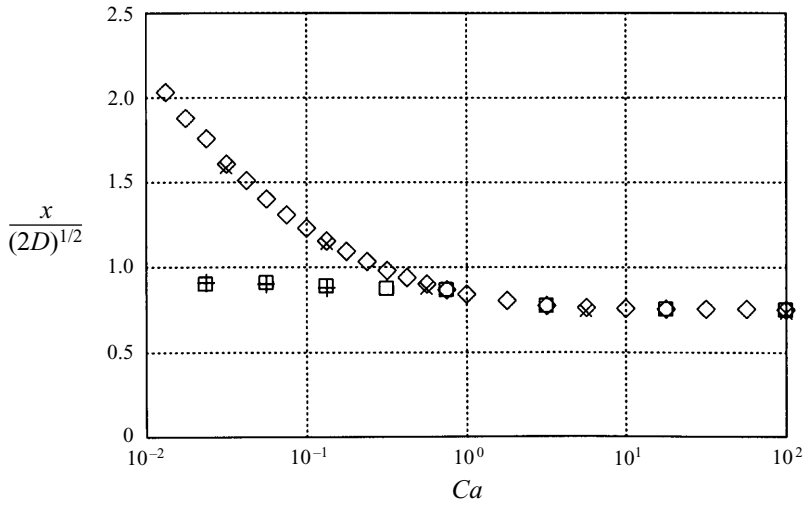

FIGURE 22. Film split location, x_s^{2D}, as a function of Ca for $D = 200$: $\diamond$, this study; $\times$, Coyle *et al.* (1986). First stagnation point downstream from the nip, x_1^{2D}: $\square$, this study; $+$, Coyle *et al.* (1986).

6. Three-dimensional results

In this section we present simulation results for the unsteady three-dimensional free-surface fluid flow problem. The calculations serve the purpose of demonstrating our three-dimensional simulation methodology, and validating and quantifying the framework of §3. We first present the evolution from a perturbed unstable two-dimensional steady flow geometry to a stable three-dimensional steady ribbed state, and compare these results with the 'predictions' of the analysis of §3. Both unsteady (§6.1) and steady (§6.2) issues are addressed. We then further validate our ribbing interpretation through a parametric (Ca) investigation of steady ribbed results (§6.3). Finally, in §6.4, we briefly discuss nonlinear state selection through variation of the boxsize.

6.1. *Nonlinear evolution to steady ribbed states*

To allow for adequate visualization of the meniscus and the ribs during the evolution towards the steady state, we consider the case of $D = 200$ (with $Re = 10^{-2}$ in (2.1)); the critical conditions for this geometry (and $Re = 0$) reported by Coyle *et al.* (1990*b*) are $Ca_c = 0.32$ and $\beta_c = \pi/30$. We present results for the following set of parameters: $D = 200$, $Ca = 3.14 \gg Ca_c = 0.32$, and $b = \lambda_c/3 = 10$ (note that $\beta = 3\,\beta_c$ is presumed to correspond to, and is in fact, an unstable mode).

The evolution of the free-surface geometry from the unstable two-dimensional steady state to the stable three-dimensional ribbed state is shown in figure 23. Full domain (non-y-symmetrized) simulations at selected D, Ca, b yield effectively identical results to the symmetric calculations (Gurfinkel Castillo 1995). Before analysing the solution in more detail, we address certain numerical issues: adaptive spanwise (z) resolution; (x, y, z) spatial resolution; and the stopping criterion. Note that temporal resolution is not an issue since the timestep used is (unfortunately) very small owing to numerical stability considerations (Ho 1989).

To demonstrate the independence of the evolution towards the steady state with respect to spanwise resolution, this and other selected 'representative' cases are repeated using the final (high) resolution mesh $\{15, 6, 5\}$ during the entire evolution,

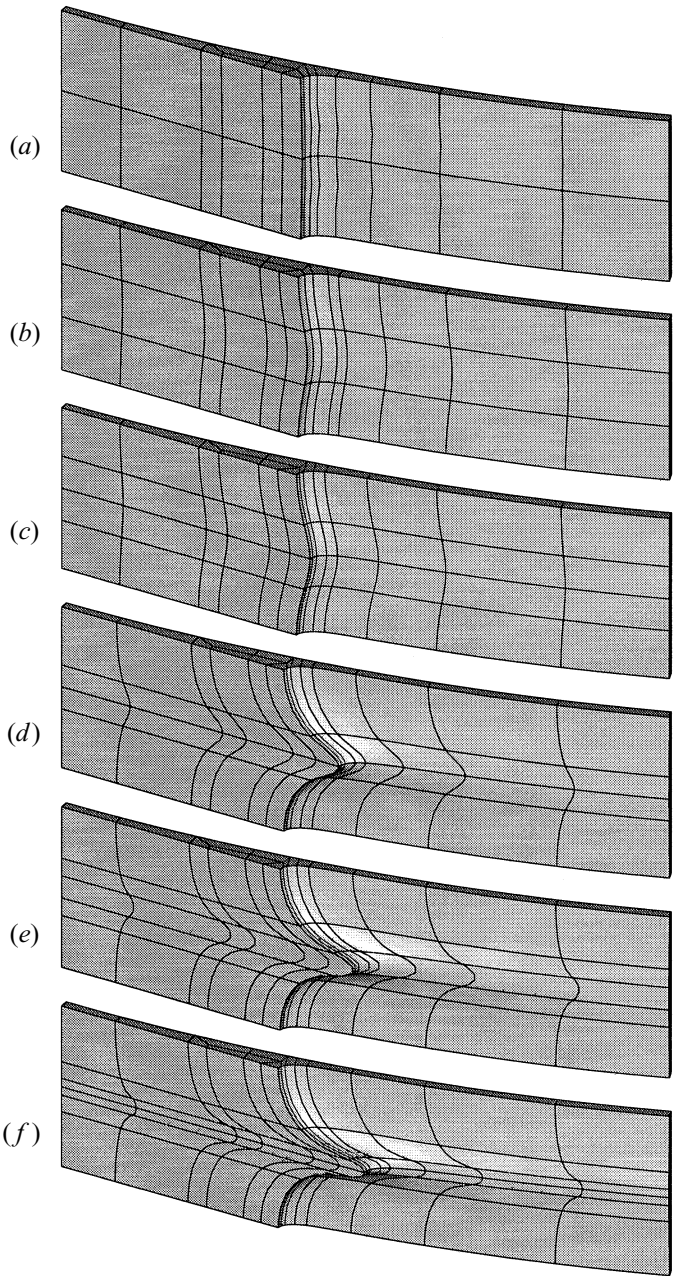

FIGURE 23. Spanwise-adaptive simulation of the evolution to a steady three-dimensional ribbed state for $D = 200$, $Ca = 3.14$, and $b = 10$: (*a*) $t = 0$, (*b*) 22, (*c*) 26, (*d*) 30, (*e*) 40, (*f*) 48. Note that, for much of the calculation, only three or four z-levels are required.

as shown in figure 24. The ratio of the computational time to perform the simulation shown in figure 24 to the time to perform the spanwise-adaptive simulation shown in figure 23 is roughly 10: the computer time on 16 nodes of an Intel i860 Hypercube required for the high-resolution simulation is approximately 800 hours, compared to approximately 80 hours for the adaptive case. Note that, owing to the distortion near the meniscus, neither simulation could be successfully completed without the

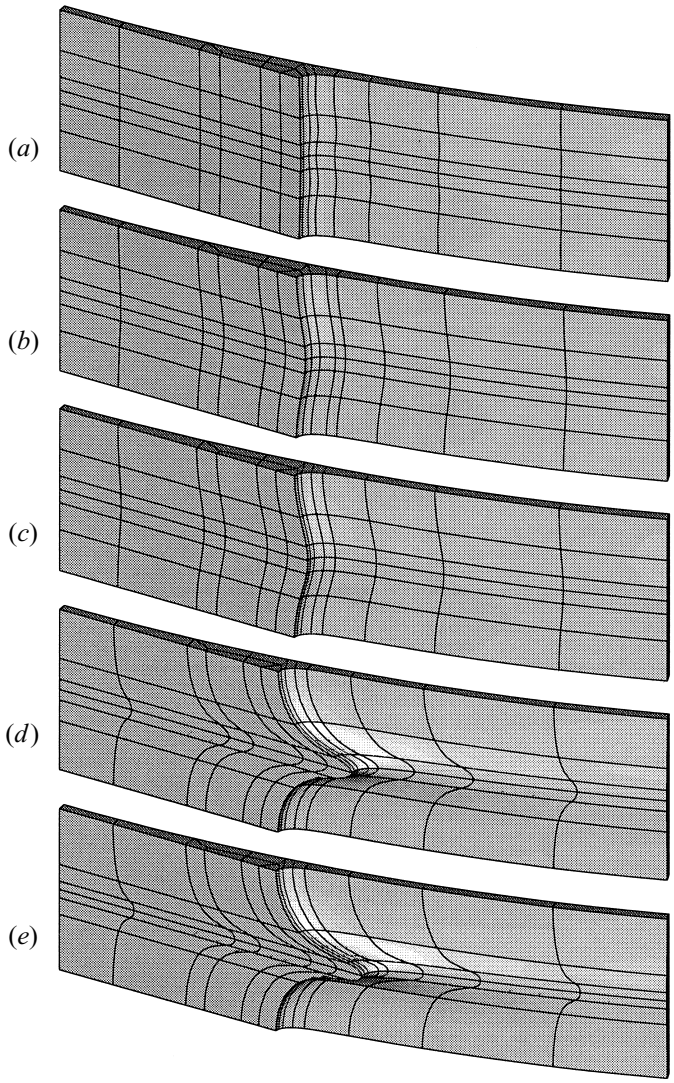

FIGURE 24. Uniformly high-resolution simulation, $\{15, 6, 5\}$, of the evolution to a steady three-dimensional ribbed state for $D = 200$, $Ca = 3.14$, and $b = 10$: (*a*) $t = 0$, (*b*) 22, (*c*) 30, (*d*) 40, (*e*) 48. The steady state shown in (*e*) is nearly identical to the steady ribbed state shown in figure 23(*f*).

remeshing techniques presented in §4.2.3. The remeshing, performed on a serial workstation, requires on the order of 100 additional hours for both the high- and adaptive-resolution simulations.

In order to verify the independence of the ribbed geometry with respect to (x, y, z) final resolution, the solution of figure 23 is mapped (see §4.2.3) onto a finer mesh, $\{15, 8, 7\}$, with approximately 350 000 degrees of freedom. The governing equations are then further integrated in time until the (in fact, a slightly tighter) stopping criterion is again satisfied. The two geometries differ only very slightly (Gurfinkel Castillo 1995). We also note that Galerkin spectral element spatial discretization generally rewards inadequate resolution with oscillations corresponding (roughly) to the highest-order polynomial that can be represented by the discrete space. We use

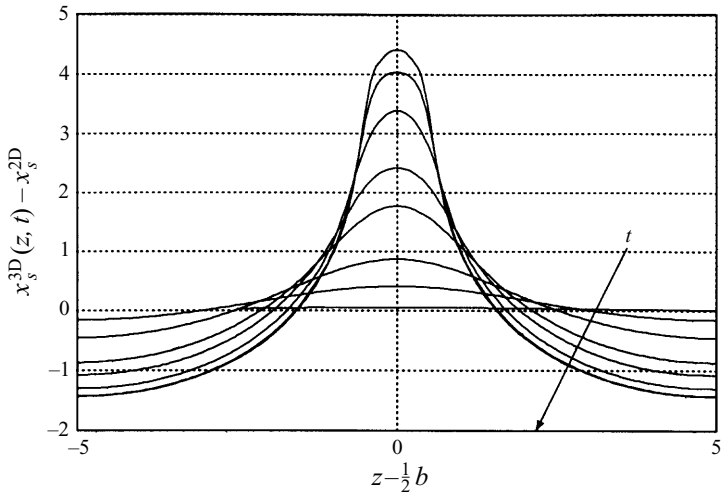

FIGURE 25. Evolution of the meniscus profile at the mid-plane, $\partial\Omega_4 \bigcap \partial\Omega_5$, for the $D = 200$, $Ca = 3.14$, and $b = 10$ simulation of figure 23. The times plotted are $t = 0$, 12, 22, 26, 31, 41, 44, 46, 48, and 60.

this symptom as an indication that remeshing is required; all results presented are essentially oscillation-free.

For the 130 000 degrees-of-freedom resolution $\{15, 6, 5\}$ calculation, the free-surface-velocity-based stopping criterion is satisfied near $t \approx 48$, at which point we deem the geometry to have achieved a steady state. In order to verify the independence of the ribbed geometry with respect to the stopping criterion, the maximum allowable normal free-surface velocity is reduced by 50% and the governing equations are then further integrated in time until this tighter stopping criterion is satisfied, at $t \approx 49$. The resulting free-surface geometry differs from the $t \approx 48$ case only near the rib tip, at which location changes in primarily the high spanwise wavenumbers conspire to increase the rib amplitude. It is possible that these tips continue to slowly grow, evolving to a different shape at very long times; however based on the spanwise Fourier analysis given below, we do not believe that this will, in fact, occur.

From this (albeit somewhat limited) series of tests at a difficult parameter value (high Ca), we believe that both our three-dimensional transient and steady solutions are accurate to within several percent in all relevant norms. With more efficient numerical procedures, such as implicit timestepping techniques and 'direct' solution strategies similar to those employed in our two-dimensional calculations, more extensive convergence studies can, and should, be performed. However, certainly at low Ca, and even at very supercritical Ca, we do not believe that any of our conclusions are the result of numerical artifacts.

We now turn to a more thorough interrogation of the time-dependent solution. The evolution of the meniscus geometry from the unstable two-dimensional steady state to the stable three-dimensional ribbed steady state is shown in figure 25. The profiles, $x_s^{3D}(z,t)$, correspond to the intersection of the free surface with the symmetry plane, $\partial\Omega_4 \bigcap \partial\Omega_5$, at different times, t. For this highly supercritical Ca, the initially very small higher spanwise harmonics attain significant amplitude as the rib achieves finite amplitude. This, in turn, is reflected in the steepening of the ribs as the steady state is approached.

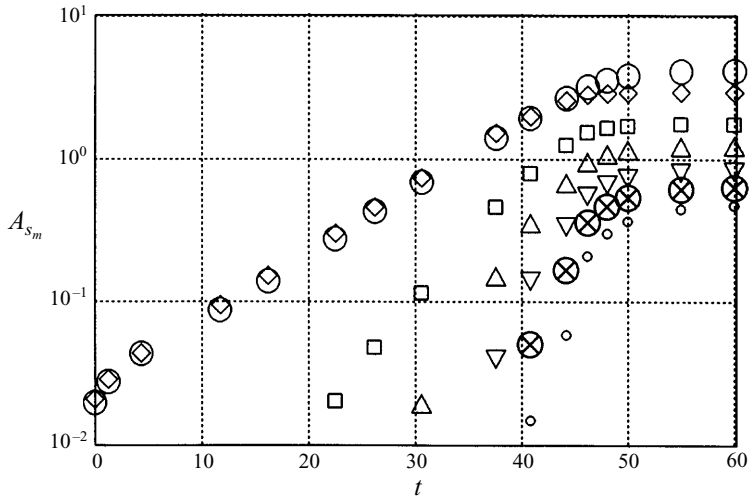

FIGURE 26. Time evolution from the perturbed unstable two-dimensional steady-state profile to the three-dimensional stable steady state, for $D = 200$, $Ca = 3.14$, and $b = 10$. We present the meniscus profile amplitude at the mid-plane, $A_{s_0}(t) = \left(\max_z x_s^{3D}(z,t) - \min_z x_s^{3D}(z,t)\right)/2$ (○), and the amplitudes of the first six meniscus spanwise Fourier modes, $A_{s_m}(t)$ (wavenumbers $m\pi/b$) $m = 1$ (◇), 2 (□), 3 (△), 4 (▽), 5 (⊗) and 6 (○).

We demonstrate the growth of the harmonics in figure 26 as a plot of the temporal evolution of the total disturbance amplitude, $A_{s_0}(t) = \left(\max_z x_s^{3D}(z,t) - \min_z x_s^{3D}(z,t)\right)/2$, and of the amplitudes of the first six meniscus Fourier modes, $A_{s_m}(t)$, obtained by performing a spanwise (z) Fourier transform of $x_s^{3D}(z,t)$. During most of the evolution toward the steady state the higher-wavenumber modes are not appreciable; they do become important, however, as the steady state is approached, consistent with the steepening of the rib observed in figure 25. The data in figure 25 at times $t \approx 48$ and $t \approx 49$ correspond to geometries that satisfy the normal and tightened stopping tolerances, respectively, described above. The equations of motion are then even further integrated in time, to $t = 60$, to verify that the stopping criterion used is adequate. Figure 26 clearly shows that, at $t = 48$, all the modes have indeed saturated, with the exception of the very highest wavenumbers; these modes continue to grow slightly, finally equilibrating (at least for $m < 25$, for which the amplitude is already small) by $t \approx 60$. (For rollers with $D = 20$ cm rotating at 12 r.p.m., the time constant for rib growth for $Ca = 3.14$ would be of the order of $50H^*/V^* \approx 0.04$s, which is consistent with experimental observation.) For the lower-Ca cases studied, even the highest-wavenumber components are unambiguously saturated upon satisfying our stopping criterion.

6.2. *Properties of the steady ribbed state*

In the previous subsection we confirmed the unstable nature of the two-dimensional steady flow geometry for the supercritical Ca considered, and described the evolution to the stable three-dimensional ribbed state. We now concentrate on the structure of the stable three-dimensional steady ribbed state in order to quantify the coupling between the meniscus instability and the ribs downstream. In particular, we wish to compute the lengths of the regions identified in §3.

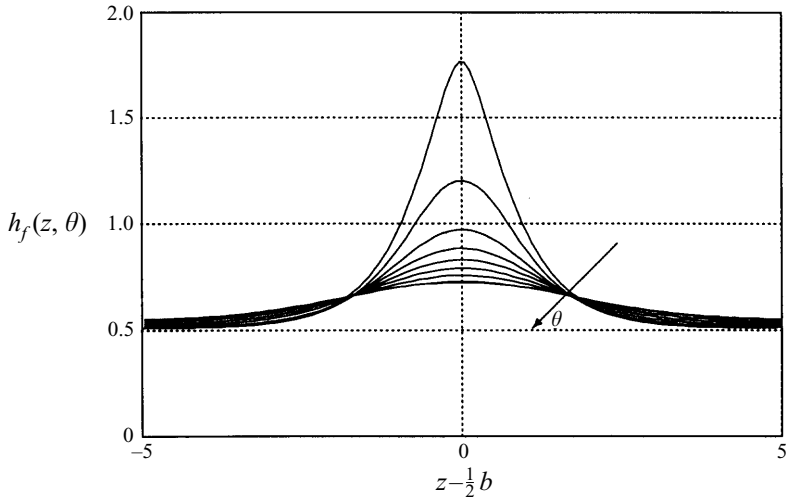

FIGURE 27. Steady free-surface profiles for $D = 200$, $Ca = 3.14$, and $b = 10$, as a function of downstream position: $\theta = 10.35°$, 11°, 12°, 13°, 14°, 15°, 16°, 17°, 18° (the sharp profile for $\theta = 10.35°$ is an artifact of the radial projection). Note that $h_f(z,\theta) \to Q/2$ sufficiently far downstream.

6.2.1. *Downstream ribs*

As described in §3, the meniscus geometry controls the free-surface profile everywhere, and we thus expect to observe ribs downstream from the meniscus. Since the view and lighting in figure 23 does not clearly show the ribs downstream on the rollers, we present in figure 27 profiles of the steady three-dimensional free surface, $h_f(z,\theta)$, at different downstream locations θ. In figure 28 we display the amplitude of the rib, given by $A_{h_0}(\theta) = \left(\max_z h_f(z,\theta) - \min_z h_f(z,\theta)\right)/2$. As expected, the rib amplitude decreases with distance from the nip; note the significant, but localized, effect of the outflow boundary condition on the flow geometry ($A_{h_0} \to 0$ as $\theta \to \theta_{\partial\Omega_3} \approx 20.4°$).

6.2.2. *Transition of flow fields: diverging to levelling*

The decrease in amplitude of the ribs for increasing θ indicates the transformation of the spanwise fluid flow pattern from a rib-sustaining diverging flow field (region I of §3) to the convergent field of the levelling film (region III of §3). Figure 29 shows the dependence of the free-surface spanwise velocity on the downstream position; clearly, in the transition region (region II of §3) between $\theta = 12°$ and $\theta = 13°$, the nature of the spanwise velocity profile changes – the spanwise velocity no longer feeds the crest of the rib, but rather, begins to drain fluid away. This is clearly seen in figure 30, in which we present the spanwise velocity direction at θ-slices of the domain Ω corresponding to the meniscus, transition, and levelling regions suggested by the schematic in figure 7. From figure 30 we can bound the extent of the transition region L_t, by $L_t \approx (D/2)\,\pi\,(13° - 12°)/180 \approx 1.75$, which is, indeed, order unity.

6.2.3. *Levelling of ribs*

We now study the levelling of the nonlinear ribs as final confirmation of the behaviour described in §3. The levelling problem is, to first order, linear, and thus the interaction between modes can be neglected. Figure 31 shows the dependence of the total rib amplitude, $A_{h_0}(\theta)$, and of the amplitude of the individual spanwise Fourier modes, $A_{h_m}(\theta)$, $m = 1,\ldots,4$, of $h_f(z,\theta)$ as a function of the roller angle, θ.

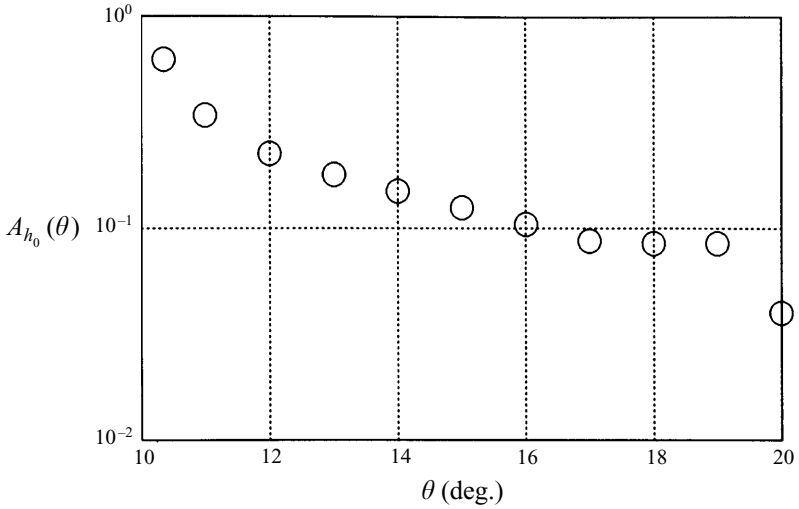

FIGURE 28. Evolution of total rib amplitude A_{h_0} ($\bigcirc$) for $D = 200$, $Ca = 3.14$, and $b = 10$, as a function of the roller angle θ. The effect of the outflow boundary condition is localized near $\theta = \theta_{\partial\Omega_3}$.

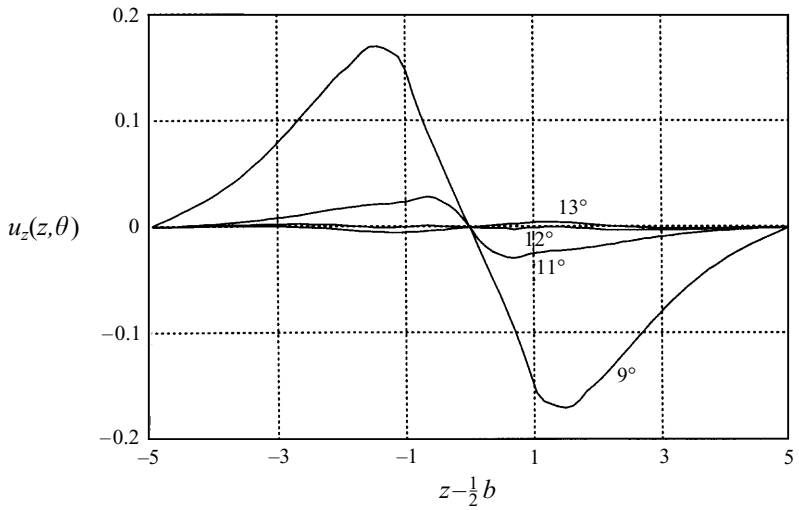

FIGURE 29. Steady free-surface spanwise velocity profiles, $u_z(z,\theta)$, at different downstream positions $\theta = 9°, 11°, 12°, 13°$ for $D = 200$, $Ca = 3.14$, and $b = 10$.

In figure 31, the absolute value of the slopes define the lengthscale over which the individual mode amplitudes will persist. As the ribs move downstream, the total rib amplitude asymptotically approaches, from above, that of the lowest-wavenumber mode, as higher-wavenumber modes decay at a faster rate. This is more clearly observed in figure 32, in which the magnitudes of the spatial decay, L_{ℓ_m}, are plotted as a function of the corresponding film wavenumber, $\beta_h = m\,2\,\pi\,h_{\mathrm{IV}}/b = m\,2\,h_{\mathrm{IV}}\,3\,\beta_c$. The magnitude of the slopes presented in figure 32 are calculated at a given downstream location, $\theta = 16°$, which is unambiguously in the levelling region yet sufficiently far upstream of outflow. The results for L_{ℓ_m} in figure 32 are seen to be in good agreement with the prediction of (3.3).

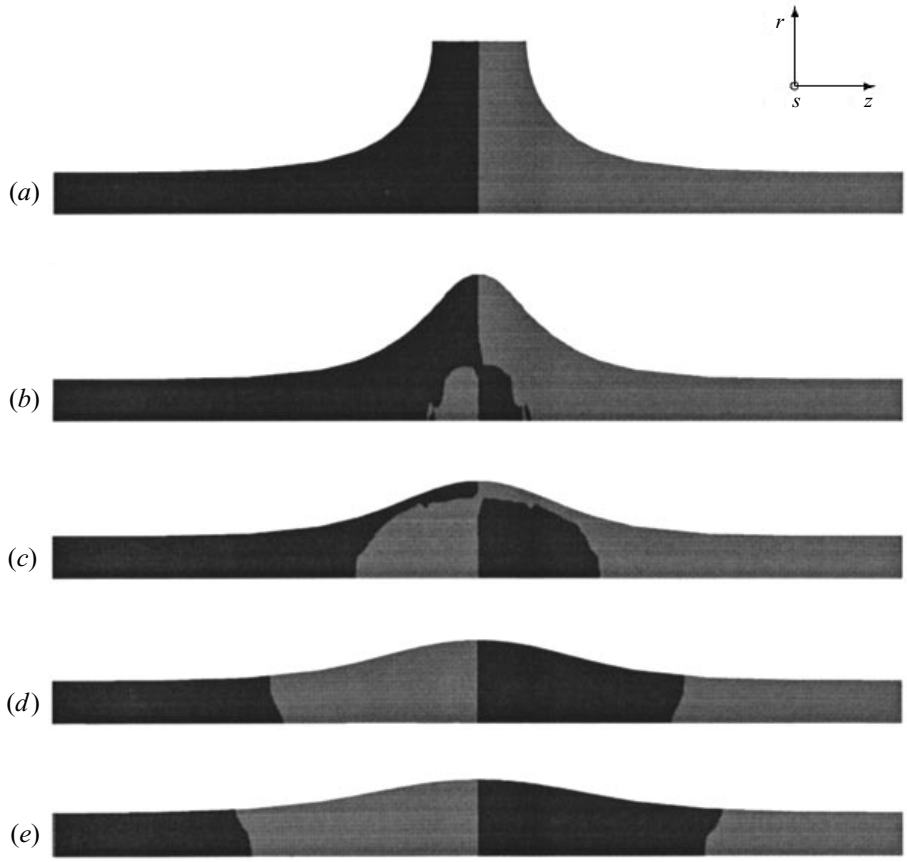

FIGURE 30. Characteristic spanwise velocity (u_z) contours for $D = 200$, $Ca = 3.14$, and $b = 10$, for: (a) meniscus region, $\theta = 10°$; (b) transition region (beginning), $\theta = 12°$; (c) transition region (end), $\theta = 13°$; (d, e) levelling region, $\theta = 14°$ and $15°$. Legend: black $u_z > 0$; grey $u_z < 0$.

Note that the decay lengthscale of the total amplitude of the ribs will be a weighted average over all wavenumbers, and will thus underpredict rib persistence if the rib profile is not monochromatic. For correct experimental verification of rib persistence, the complete rib profile must be determined at different downstream locations, or measurements of the total amplitude must be made sufficiently far downstream that the rib profile is monochromatic. At present, available experimental data for ribs (Hasegawa & Sorimachi 1993) are based on an assumed rib profile, and are measured at an indeterminate downstream location θ.

6.3. *The effect of capillary number*

The results presented above are all for one combination of the governing parameters, $D = 200$, $Ca = 3.14$, and $b = 10$. We now present the characteristics of steady three-

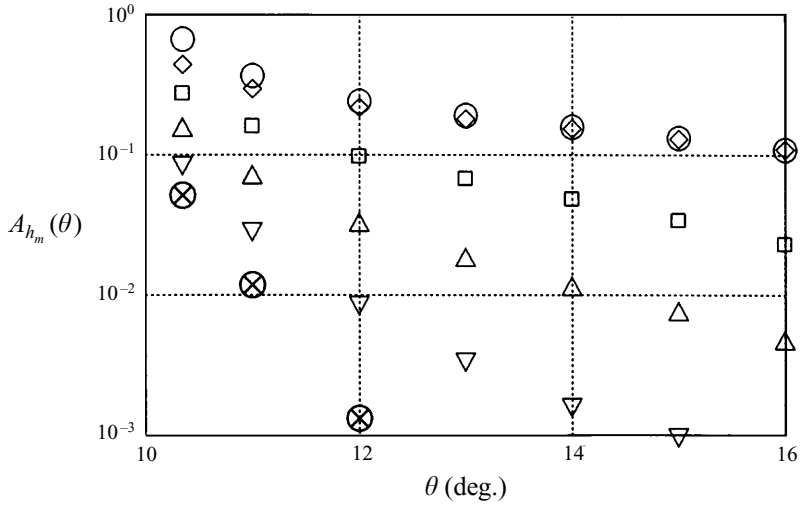

FIGURE 31. Dependence of rib amplitude $A_{h_0}(\theta)$ (◯), and of the amplitude, $A_{h_m}(\theta)$, of the profile spanwise Fourier modes with film wavenumber $\beta_h = m(2\pi h_{\mathrm{IV}}/b)$, $m = 1$ (◇), 2 (□), 3 (△), 4 (▽), and 5 (⊗) as a function of roller angle θ for $D = 200$, $Ca = 3.14$, and $b = 10$.

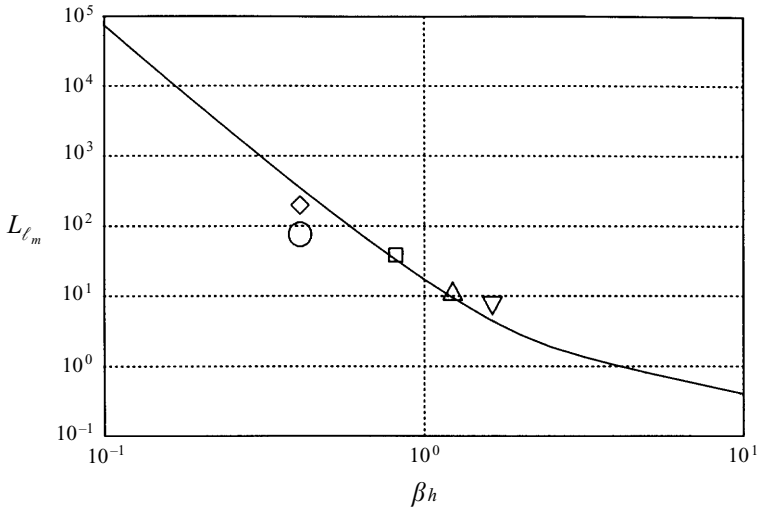

FIGURE 32. Levelling-region lengthscale, L_{ℓ_m}, for the rib (◯), and for the first four profile spanwise Fourier modes with wavenumbers $\beta_h = m(2\pi h_{\mathrm{IV}}/b)$, $m = 1$ (◇), 2 (□), 3 (△), 4 (▽); the solid line is based on (3.3). As for all results in this subsection, $D = 200$, $Ca = 3.14$, and $b = 10$.

in the speed of the rollers, in that we continue our results in Ca to achieve the set of equilibria shown in figure 33. As expected, as Ca is increased, in addition to the two-dimensional migration of the meniscus towards the nip described in §5, there is a monotonic increase in three-dimensional rib amplitude and in rib steepness. Figure 33 also suggests that as Ca is increased, the meniscus profile approaches a very steep square-cell shape similar to that observed in viscous fingering as $Ca \to \infty$ (Rabaud *et al.* 1991).

In order to quantify the harmonic content of the meniscus rib profiles we extract

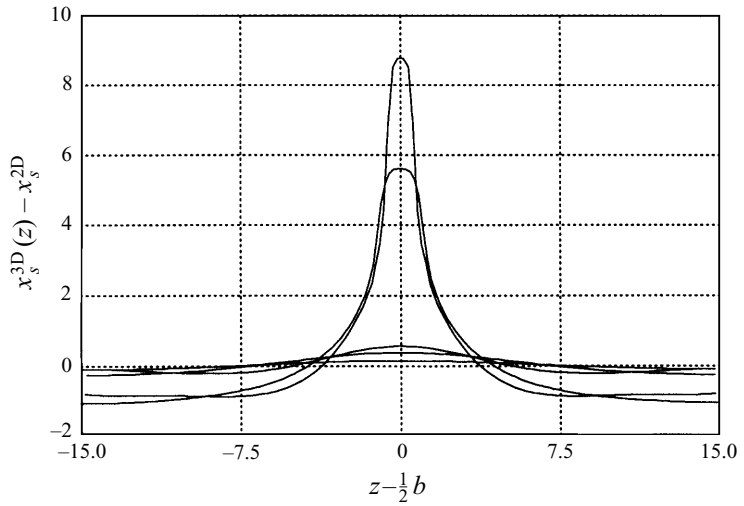

FIGURE 33. Steady-state profiles of $\partial\Omega_4 \bigcap \partial\Omega_5$ for $D = 200$, $b = \lambda_c = 30$ and $Ca = 0.5$, 0.75, 1, 3.14, and 5. The ribs exhibit increasing amplitude, A_{s_0}, and greater harmonic content with increasing Ca (roller velocity).

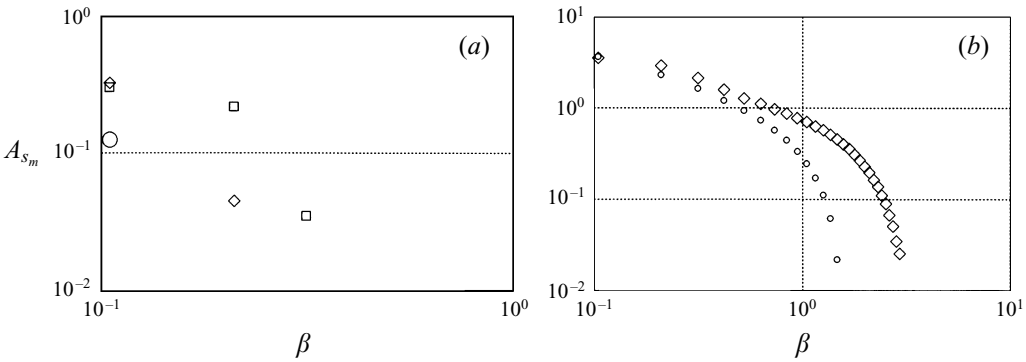

FIGURE 34. Amplitude of the spanwise Fourier modes of the steady-state profiles of $\partial\Omega_4 \bigcap \partial\Omega_5$, A_{s_m}, for $D = 200$, $b = 30$, as a function of the corresponding Fourier mode wavenumber $\beta = m\beta_c$. (*a*) $Ca = 0.5$ (○), 0.75 (◇), and 1 (□) (for wavenumbers higher than those shown, the amplitude is uniformly less than 10^{-3}); (*b*) $Ca = 3.14$ (○) and 5 (◇).

the amplitudes of the spanwise Fourier modes of each profile. Figures 34(*a*) and 34(*b*) show the amplitudes of the Fourier modes as a function of their corresponding wavenumber for moderately supercritical and highly supercritical Ca, respectively. The rib profiles for the moderately supercritical Ca are essentially monochromatic (figure 34*a*) while the profiles for highly supercritical Ca ($Ca \gg Ca_c$) exhibit significant harmonic content (figure 34*b*). The convergence of the profiles to an asymptotic form for increasing Ca is again suggested by the low-wavenumber similarity of the two solutions presented in figure 34*b*. The stopping criterion used possibly affects the accuracy of the predicted steady-state amplitude of the higher-wavenumber Fourier modes; we believe that for the cases studied this error is minor (see §6.1).

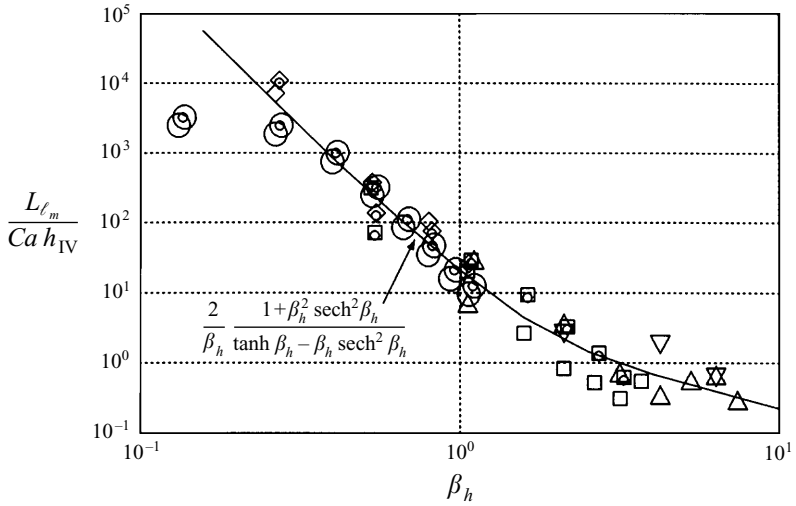

FIGURE 35. Levelling-region length, L_{ℓ_m}, of the Fourier modes of the rib profile as a function of spanwise wavenumber, $\beta_h = m(2\pi\, h_{\mathrm{IV}}/b)$, for $D = 200$, $b = 30/2^{n-1}$, and $Ca = 1$, $n = 1$ (◎), 2 (◈), 3 (⧈), 4 (⧋), and $Ca = 5$, $n = 1$ (○), 2 (◇), 3 (□), 4 (△), 5 (▽). The solid line is based on (3.3).

6.3.2. *Transition and levelling of ribs*

We have determined that, for the cases considered here, the transition region length L_t, estimated as in §6.2.2, is indeed $O(1)$. Neither our definition nor our calculation procedure for L_t are sufficiently precise to warrant further elaboration here.

We now turn to levelling. Following procedures similar to those used to construct figure 32, we collect in figure 35 the quantity $L_{\ell_m}/(Ca\,h_{\mathrm{IV}})$ for several of the ribbed geometries obtained (note we also include numerous results for box sizes other than $b = \lambda_c$). The quantity $L_{\ell_m}/(Ca\,h_{\mathrm{IV}})$ should be a function only of spanwise Fourier mode film wavenumber $\beta_h = m\,2\pi\, h_{\mathrm{IV}}/b$, as confirmed in figure 35. Furthermore, there is very good agreement with the predictions of (3.3), save at very low wavenumbers. We conjecture, but do not yet have conclusive evidence, that the latter discrepancy is due to low signal-to-noise ratios, as the decay rates are very small as $\beta_h \to 0$.

6.4. *Nonlinear state selection*

We now present results for $D = 200$ and $Ca = 0.5$ in order to show the effect of the box size b and the history of the flow on the resulting steady ribbed geometry and flow field. We consider the computationally simpler case of a slightly supercritical Ca, in particular, $Ca = 0.5$; recall that Coyle *et al.* (1990*b*) report $Ca_c = 0.32$ and $\lambda_c = 30$ for $D = 200$.

Figure 36 shows the steady-state profiles of $\partial\Omega_4 \bigcap \partial\Omega_5$ as a function of the box size $b = \lambda_c/2^{n-1}$ for $n = 1, \ldots, 3$, in each case beginning with initial conditions as described in §4.2.4. We observe that the high-wavenumber cutoff is less than $4\,\beta_c = 4\,\pi/30$ since the rib amplitude for $b = \lambda_c/4$ vanishes. We next considered b greater than λ_c, and found that it proved impossible to obtain a one-rib stable ribbed geometry with $b = 2\,\lambda_c$. Furthermore, if we take as initial condition a two-ribbed state created by periodically replicating our one-rib $b = \lambda_c$ state of figure 36 (thus considering $b = 2\,\lambda_c$), the flow evolves to a two-ribbed $b = 2\,\lambda_c$ steady state which differs from the replicated $b = \lambda_c$ initial condition only in the presence of a very small (nonlinearly generated) subharmonic $\beta = \beta_c/2$ component.

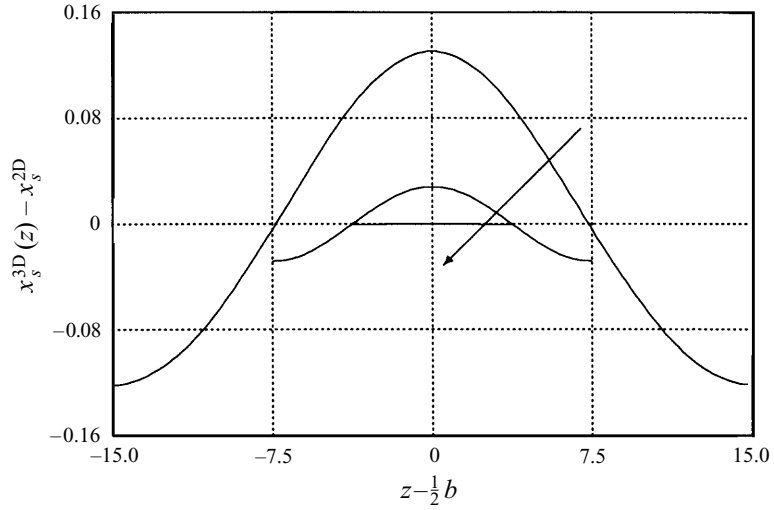

FIGURE 36. Steady-state profiles of $\partial\Omega_4 \bigcap \partial\Omega_5$ for $Ca = 0.5$, $D = 200$, and $b = 30/2^{n-1}$, for $n = 1, \ldots, 3$ and $z \in [0, b]$.

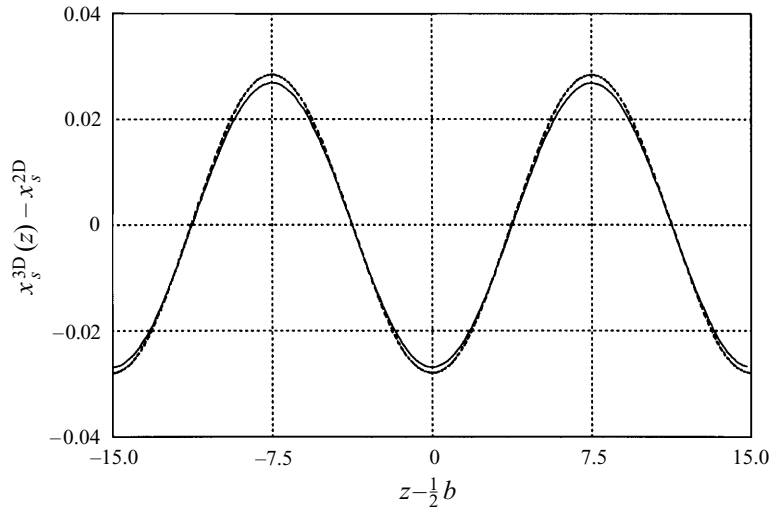

FIGURE 37. Steady-state profile of $\partial\Omega_4 \bigcap \partial\Omega_5$ for $D = 200$ and $Ca = 0.5$ for $b = \lambda_c = 30$ (solid line) for an initial condition corresponding to a slight perturbation of a periodically replicated one-rib $b = \lambda_c/2$ steady state (dashed line).

We have thus observed that we cannot obtain a one-rib steady state for $Ca = 0.5$ and $D = 200$ and $b = 2\lambda_c$, but that it is simple to obtain a two-rib solution. It is then natural to ask whether we can produce a two-rib $b = \lambda_c$ state rather than a one-rib $b = \lambda_c$ solution by choosing as an initial condition a two-rib profile; the answer is affirmative. We show in figure 37 the (stable) two-ribbed $b = \lambda_c$ steady-state solution that results from an initial condition which is a slight perturbation of a periodically replicated one-rib $b = \lambda_c/2$ steady profile. As expected, the two-rib $b = \lambda_c$ solution and the replicated one-rib $b = \lambda_c/2$ steady state differ slightly in low-wavenumber content. More importantly, however, the two-rib $b = \lambda_c$ steady state

clearly represents a different solution than the one-rib $b = \lambda$

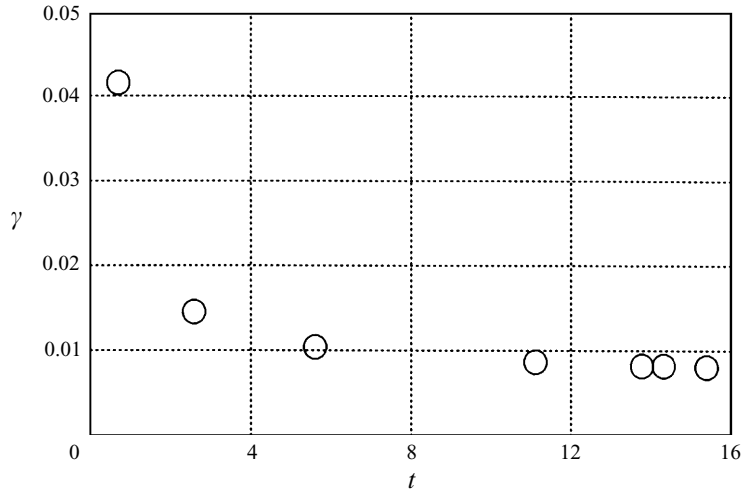

FIGURE 38. Spectral element prediction of the growth-rate γ for an unstable perturbation for $D = 40$, $Ca = 15$, and $b = 9$. Coyle *et al.* (1990*b*) predict $\gamma \approx 0.01$.

dimensional scheme, the development of better outflow boundary conditions, and the extension of the remeshing schemes to allow for greater topological variation – but also on the physical side – e.g. the development of a better understanding of state selection, the consideration of a larger range of parameters, the study of end effects, and the extension to non-Newtonian working fluids. Only then can our results be directly applied to practical systems of interest.

The authors would like to thank Drs Lee Ho, Einar Rønquist, and Edward Bullister of Nektonics, Inc., and Professor Paul Fischer of Brown University, for their help in applying the spectral element solver NEKTON^{TM} to our film-coating study, and to Fluent, Inc. for NEKTON^{TM} support. We would also like to thank Professors Robert A. Brown and Ain A. Sonin of MIT, Dr Dennis Coyle of General Electric, and Dr S. Subbiah of Fluent, Inc. for valuable comments and suggestions. Finally, we thank the reviewers for their careful observations and recommendations.

This work was supported by the Defense Advanced Research Projects Agency under Grant N00014-91-J-1889, by the Office of Naval Research under Grants N00014-90-J-4124 and N00014-89-J-1610, and by Intevep S.A., an affiliate of Petróleos de Venezuela.

Appendix. Linear stability numerical test

In §5 we validate our nonlinear two-dimensional methods by comparison with the results of Coyle *et al.* (1986). No nonlinear three-dimensional results are available, so we limit our numerical tests to the linear stability predictions of Coyle *et al.* (1990*b*). (The levelling results of figure 26 also serve as a consistency check, albeit somewhat indirect and circular.) Note that our numerical methods are a very inefficient means by which to perform linear stability analysis, especially near criticality; we present this comparison only to demonstrate that our spectral element methods accurately compute a known three-dimensional time-dependent solution.

In Coyle *et al.* (1990*b*), growth rates are given for three-dimensional disturbances to the two-dimensional steady states. For $D = 40$, $Ca = 15$, and $\beta = \pi/9$, the reported

growth rate γ is slightly less than 0.01 (appropriately scaled from figure 25 of Coyle *et al.* 1990*b*). In figure 38 we present the time evolution of our prediction for γ, computed as

$$\frac{\ln A_{s_0}(t+\Delta t) - \ln A_{s_0}(t-\Delta t)}{2\Delta t}$$

with $\Delta t \approx 2\times 10^{-4}$, for the evolution of a three-dimensional disturbance from an initial amplitude of $A_{s_0} = 0.005$. As expected, the growth rate rapidly converges to a value near 0.01, in agreement with the result of Coyle *et al.* (1990*b*). (Note it is not clear in Coyle *et al.* (1990*b*) which boundary conditions are applied on the three-dimensional disturbance at inflow; in our direct-simulation approach, the perturbation satisfies, to first order, the homogeneous version of (2.2).)

REFERENCES

Benkreira, H., Edwards, M. & Wilkinson, W. 1982 Ribbing instability in the roll coating of Newtonian fluids. *Plastics Rubber Proc. Applics.* **2**, 137–144.

Bruyn, J. & Pan, L. 1995 Delayed onset of ribbing instability due to finite-size effects. *Phys. Fluids* **7**, 2185–2190.

Canedo, E. L. & Denson, C. D. 1989 Flow in driven cavities with a free surface. *AIChE J.* **35**, 129–38.

Christodolou, K. & Scriven, L. 1989 The fluid mechanics of slide coating. *J. Fluid Mech.* **208**, 321–354.

Cohen, E. & Gutoff, E. 1992 *Modern Coating and Drying Technology*. VCH Publishers, New York.

Coyle, D. 1992 Roll coating. In *Modern Coating and Drying Technology* (ed. E. D. Cohen & E. B. Gutoff), chap. 3, pp. 63–115. VCH Publishers, New York.

Coyle, D., Macosko, C. & Scriven, L. 1986 Film splitting flows in forward roll coating. *J. Fluid Mech.* **171**, 183–208.

Coyle, D., Macosko, C. & Scriven, L. 1990*a* The fluid dynamics of reverse roll coating. *AIChE J.* **36**, 161–174.

Coyle, D., Macosko, C. & Scriven, L. 1990*b* Stability of symmetric film-splitting between counter-rotating cylinders. *J. Fluid Mech.* **216**, 437–458.

Decré, M., Gailly, E. & Buchlin, J.-M. 1995 Meniscus shape experiments in forward roll coating. *Phys. Fluids* **7**, 458–467.

Donea, J. 1983 Arbitrary Lagrangian-Eulerian finite element methods. In *Computational Methods for Transient Analysis* (ed. T. Belytschko & T. Hughes), chap. 10. North Holland.

Dowson, D. & Taylor, C. 1979 Cavitation in bearings. *Ann. Rev. Fluid Mech.* **11**, 35–66.

Dussan V., E. & Davis, S. 1986 Stability in systems with moving contact lines. *J. Fluid Mech.* **173**, 115–130.

Fischer, P. F. & Patera, A. T. 1991 Parallel spectral element solution of the Stokes problem. *J. Comput. Phys.* **92**, 380–421.

Fischer, P. F. & Patera, A. T. 1994 Parallel simulation of viscous incompressible flows. *Ann. Rev. Fluid Mech.* **26**, 483–527.

Gurfinkel Castillo, M. E. 1995 Modelling and parallel simulation of three–dimensional ribbing instability in symmetric forward-roll coating processes. PhD thesis, Massachusetts Institute of Technology.

Gutoff, E. B. 1993 Avoid coating and drying defects. *Chem. Engng Prog.*, Jan, 49–55.

Hakim, V., Rabaud, M., Thomé, H. & Couder, Y. 1990 Directional growth in viscous fingering. In *New Trends in Nonlinear Dynamics and Pattern-Forming Phenomena* (ed. P. Huerre), vol. 237, pp. 327–337. Plenum.

Hasegawa, T. & Sorimachi, K. 1993 Wavelength and depth of ribbing in roll coating and its elimination. *AIChE J.* **39**, 935–945.

Ho, L. 1989 A Legendre spectral element method for simulation of incompressible unsteady viscous free-surface flows. PhD thesis, Massachusetts Institute of Technology.

Ho, L.-W. & Patera, A. T. 1990 A Legendre spectral element method for simulation of unsteady incompressible viscous free-surface flows. *Comput. Meth. Appl. Mech. Engng* **80**, 355–366.

Ho, L.-W. & Patera, A. T. 1991 Variational formulation of three dimensional viscous free-surface flows: Natural imposition of surface tension boundary conditions. *Intl J. Numer. Meth. Fluids* **13**, 691–698.

Ho, L.-W. & Rønquist, E. 1992 Spectral element solution of steady incompressible viscous free-surface flows. In *Proc. Intl Conf. on Spectral and High Order Methods for Partial Differential Equations, Le Corum, Montpellier, France*, pp. 347–367. North-Holland.

Kheshgi, H. S. 1989 Profile equations for film flows at moderate Reynolds numbers. *AIChE J.* **35**, 1719–1727.

Kistler, S. & Scriven, L. 1983 Coating flows. In *Computational Analysis of Polymers* (ed. J. Pearson & S. Richardson), chap. 8, pp. 243–299. Barking, Essex, England.

Kistler, S. & Scriven, L. 1994 The teapot effect: sheet-forming flows with deflection, wetting and hysteresis. *J. Fluid Mech.* **263**, 19–62.

Lee, K.-Y., Liu, L.-D. & Liu, T.-J. 1992 Minimum wet thickness in extrusion slot coating. *Chem. Engng Sci.* **47**, 1703–1713.

Levich, B. 1962 *Physicochemical Hydrodynamics.* Prentice Hall.

Maday, Y. & Patera, A. T. 1989 Spectral element methods for the Navier-Stokes equations. In *State-of-the-art Surveys on Computational Mechanics* (ed. J. Oden & A. Noor), pp. 71–143. ASME.

NEKTON^{TM} *Users Guide.* Nektonics, Inc. Version 2.85.

Mill, C. & South, G. 1967 Formation of ribs on rotating rollers. *J. Fluid Mech.* **28**, 523–529.

Orchard, S. 1962 On surface levelling in viscous liquids and gels. *Appl. Sci. Res.* **11**, 451–464.

Pearson, J. 1960 The instability of uniform viscous flow under rollers and spreaders. *J. Fluid Mech.* **7**, 481–500.

Pitts, E. & Greiller, B. 1961 The flow of thin liquid films between rollers. *J. Fluid Mech.* **11**, 33–50.

Pranckh, F. & Scriven, L. 1990 Elastohydrodynamics of blade coating. *AIChE J.* **36**, 587–597.

Probstein, R. F. 1995 *Physicochemical Hydrodynamics: An Introduction.* John Wiley and Sons.

Rabaud, M., Couder, Y. & Michalland, S. 1991 Wavelength selection and transients in the one-dimensional array of cells of the printer's instability. *Eur. J. Mech.* B/*Fluids* **10**, 253–260.

Reinelt, D. 1995 The primary and inverse instabilities of directional viscous fingering. *J. Fluid Mech.* **285**, 303–327.

Rønquist, E. 1988 Optimal spectral element methods for the unsteady three-dimensional incompressible Navier-Stokes equations. PhD thesis, Massachusetts Institute of Technology.

Rønquist, E. 1991 A domain decomposition method for elliptic boundary value problems: Application to unsteady incompressible fluid flow. In *Proc. Fifth Intl Conf. on Domain Decomposition Methods for Partial Differential Equations, Norfolk, Virginia.* (ed. D. E. Keyes, T. F. Chan, G. A. Meurant, J. S. Scroggs & R. G. Voigt), pp. 545–557. SIAM, Philadelphia.

Ruschak, K. 1980 A method for incorporating free boundaries with surface tension in finite element fluid flow simulators. *Intl J. Numer. Meth. Engng* **15**, 639–648.

Ruschak, K. 1983 A three-dimensional linear stability analysis for two dimensional free boundary flows by the finite element method. *Comput. Fluids* **11**, 391–401.

Ruschak, K. 1985 Coating flows. *Ann. Rev. Fluid Mech.* **17**, 65–89.

Saffman, P. G. 1986 Viscous fingering in Hele-Shaw cells. *J. Fluid Mech.* **173**, 73–94.

Saffman, P. G. & Taylor, G. I. 1958 The penetration of a fluid into a porous medium or Hele-Shaw cell containing a more viscous liquid. *Proc. R. Soc. Lond.* A **245**, 312–342.

Savage, M. 1977 Cavitation in lubrication. *J. Fluid Mech.* **80**, 743–768.

Taylor, G. I. 1963 Cavitation of a viscous fluid in narrow passages. *J. Fluid Mech.* **14**, 595–619.

Tsiveriotis, K. & Brown, R. 1992 Boundary-conforming mapping applied to computations of highly deformed solidification interfaces. *Intl J. Numer. Meth. Fluids* **14**, 981–1003.

Wang, F. & Domoto, G. 1994 Free surface Taylor vortices. *J. Fluid Mech.* **261**, 169–198.